

JGR Space Physics



RESEARCH ARTICLE

10.1029/2020JA028751

Understanding the Total Electron Content Variability Over Europe During 2009 and 2019 SSWs

Key Points:

- The mid-latitude Total Electron Content (TEC) variability over Europe is observed and simulated during 2009 and 2019 Sudden Stratospheric Warmings (SSWs)
- Observations and simulation results show that the TEC variability was caused predominantly by geomagnetic forcing for the 2019 SSW
- The TEC variability at European mid-latitudes due to semidiurnal solar (SW2) and lunar (M2) tidal changes during both SSWs remain within ~20%–25% of the background TEC

Supporting Information:

Supporting Information may be found in the online version of this article.









Correspondence to:

T. A. Siddiqui,
siddiqui@iap-kborn.de

Citation:

Siddiqui, T. A., Yamazaki, Y., Stolle, C., Maute, A., Laštovička, J., Edemskiy, I. K., et al. (2021). Understanding the total electron content variability over Europe during 2009 and 2019 SSWs. *Journal of Geophysical Research: Space Physics*, 126, e2020JA028751. <https://doi.org/10.1029/2020JA028751>

Received 27 SEP 2020
Accepted 26 AUG 2021

T. A. Siddiqui¹ , Y. Yamazaki² , C. Stolle^{2,3} , A. Maute⁴ , J. Laštovička⁵ ,
I. K. Edemskiy⁵ , Z. Mošna⁵ , and M. Sivakandan¹ 

¹Leibniz-Institute of Atmospheric Physics, Kühlungsborn, Germany, ²GFZ German Research Centre for Geosciences, Potsdam, Germany, ³Faculty of Science, University of Potsdam, Potsdam, Germany, ⁴High Altitude Observatory, National Center for Atmospheric Research, Boulder, CO, USA, ⁵Institute of Atmospheric Physics, Czech Academy of Sciences, Prague, Czech Republic

Abstract The nature of the variability of the Total Electron Content (TEC) over Europe is investigated during 2009 and 2019 Northern Hemisphere (NH) SSW events in this study by using a combination of Global Navigation Satellite System (GNSS) based TEC observations and Thermosphere-Ionosphere Electrodynamics General Circulation Model (TIE-GCM) simulations. To simulate the SSW effects in TIE-GCM, the dynamical fields from the Whole Atmosphere Community Climate Model with thermosphere and ionosphere extension (WACCM-X) simulations of 2009 and 2019 SSWs are specified at the TIE-GCM lower boundary. The observed and simulated TEC are in overall good agreement and therefore the simulations are used to understand the sources of mid-latitude TEC variability during both SSWs. Through comparison of TIE-GCM simulations with and without geomagnetic forcing, we find that the TEC variability during the 2019 SSW event, was predominantly geomagnetically forced, while for the 2009 SSW, the major variability in TEC was accounted for by the changes in vertically propagating migrating semidiurnal solar (SW2) and lunar (M2) tides. By comparing the TIE-GCM simulations with and without the SW2 and M2 tides, we find that these semidiurnal tides contribute to ~20%–25% increase in the quiet background TEC.

Plain Language Summary The region of Earth's upper atmosphere between the altitude range 80–1,000 km known as the ionosphere is made up of a mixture of charged and neutral gases. As the ionosphere is sandwiched between the Earth's lower atmosphere and the magnetosphere, it is prone to being influenced by the Earth's lower atmospheric weather and to the solar driven space weather. The impact of the Earth's meteorological processes on the ionosphere becomes particularly important during periods of low solar activity and one large-scale meteorological phenomenon known as Sudden Stratospheric Warming (SSW) is known to cause major changes in the ionosphere. Much of our knowledge about these ionospheric changes have come from studying the 2009 SSW event, which occurred under extremely rare quiet solar and geomagnetic conditions. Another SSW event occurred toward in 2019 under similarly rare and favorable conditions, which serves a motivation to further investigate the ionospheric impacts of SSWs. Using numerical models, we quantify the ionospheric variability that is caused by both geomagnetic and lower atmospheric forcings during both SSWs. For the 2019 SSW, the mid-latitude ionospheric variability is found to be predominantly geomagnetically forced while during the 2009 SSW it is found to be lower atmospherically forced.

1. Introduction

The axial tilt of the Earth creates a strong temperature gradient between the pole and mid-latitudes due to a lack of solar heating over the polar regions in wintertime. This temperature gradient along with the Earth's coriolis force result in the formation of stratospheric polar vortex (SPV) that appears every winter over the high-latitudes (e.g., Polvani et al., 2013). The SPV manifests itself in the form of planetary-scale eastward winds that encircle the pole at mid-to high latitudes and experiences large intra- and inter-annual variability due to interaction with the planetary waves (PWs) of tropospheric origin. When the stratospheric winds are in the eastward direction, PWs can propagate vertically up from the troposphere into the stratosphere (Charney & Drazin, 1961) and when these waves break in the stratosphere they deposit their momentum in the westward direction (McIntyre & Palmer, 1983), which leads to the deceleration of the SPV. Due to

© 2021 The Authors.

This is an open access article under the terms of the [Creative Commons Attribution-NonCommercial License](https://creativecommons.org/licenses/by-nc/4.0/), which permits use, distribution and reproduction in any medium, provided the original work is properly cited and is not used for commercial purposes.

larger topographic and land-sea contrasts, the PW activity is higher in the Northern Hemisphere (NH) as compared to the Southern Hemisphere (SH) (e.g., van Loon et al., 1973), which results in the NH SPV being weaker and much more variable than the one in the SH (Waugh & Randel, 1999). Certain extreme cases of PW activity can lead to a breakdown of the SPV and a reversal of the eastward winds resulting in magnificent transient meteorological events known as sudden stratospheric warmings (SSWs) (e.g., Matsuno, 1971; Scherhag, 1952).

SSWs are large-scale events that result in an increase in the stratospheric polar temperature usually by several tens of degrees within a few days. The increase in the polar temperature reverses the meridional temperature gradient, and concurrently, induces a deceleration of the eastward zonal mean zonal wind (ZMZW) (e.g., Andrews et al., 1987). In literature, SSWs are classified as major and minor warmings depending on the extent of increase in polar stratospheric temperature and ZMZW reversal. According to the definition of World Meteorological Organization (WMO), an SSW event is said to be “major” if the eastward zonal mean flow, poleward of 60° at 10 hPa, reverses to westward along with the reversal of the meridional temperature gradient. A “minor” SSW event occurs when there is no reversal of the eastward zonal mean flow but the polar stratospheric temperature increases by at least 25 K within a week or earlier. Major SSWs are common in the NH and occur with a frequency of 0.6/year (e.g., Butler et al., 2015; Charlton & Polvani, 2007) whereas SSWs in the SH are extremely rare. Only one major SSW event that occurred in September 2002 (e.g., Allen et al., 2003; Baldwin, 2003) and two minor SSWs occurring in August 2010 (Eswaraiah et al., 2017) and September 2019 (Yamazaki et al., 2020) have been recorded in the SH.

The SSW associated effects are not only limited to the polar stratosphere, but are rather witnessed across different latitudes and altitudes (Pedatella et al., 2018). The warming in the polar stratosphere is accompanied by cooling in the equatorial stratosphere (Fritz & Soules, 1970), warming in the equatorial mesosphere (e.g., Chandran & Collins, 2014; Garcia, 1987) and cooling in the polar mesosphere (e.g., Labitzke, 1972; Liu & Roble, 2002). The NH SSW related effects are also witnessed in the SH in the form of mesospheric warming and a decrease in the occurrence of polar mesospheric clouds through inter-hemispheric coupling mechanisms (e.g., Karlsson et al., 2009; Körnich & Becker, 2010). The associated effects of NH SSW have also been reported to result in warming in the lower thermosphere at mid- and high-latitudes (e.g., Goncharenko & Zhang, 2008; Funke et al., 2010).

In the last decade, evidence of the SSW impact in the ionosphere, mostly facilitated by extremely quiet solar and geomagnetic activity levels in the last solar cycle, have been reported in numerous studies following the seminal works by Goncharenko and Zhang (2008) and Chau et al. (2009). In response to SSWs, multi-instrument observations have revealed a consistent enhanced semidiurnal perturbation pattern at low-latitudes in ionospheric vertical plasma drifts (e.g., Chau et al., 2009), electron densities (e.g., Lin et al., 2013) and equatorial electrojet (e.g., Fejer et al., 2010; Vineeth et al., 2009; Yamazaki et al., 2012). These perturbations have been linked to the variability in migrating semidiurnal solar (SW2) and lunar (M2) atmospheric tides during SSWs. The SW2 and M2 tides are generated in the lower atmospheric regions and are able to propagate up to the dynamo-region heights where they influence the generation of electric fields in the ionosphere (Baker & Martyn, 1953). The SW2 enhancement during SSWs is thought to be due to the changes in tidal propagation conditions (Jin et al., 2012), non-linear interaction with the stationary PWs (Liu et al., 2010) and changes in the stratospheric ozone distribution (Goncharenko et al., 2012; Siddiqui et al., 2019). The cause of M2 amplification is suggested to be a result of background ZMZW changes, which shifts the secondary (Pekeris) resonance peak of the atmosphere toward the period of M2 tide (Forbes & Zhang, 2012). It has also been found during SSWs that the relative enhancement of M2 tide in mesosphere-lower thermosphere (MLT) and ionosphere is larger than that of SW2 (Pedatella et al., 2012) and the typically smaller amplitudes of M2 can even exceed those of SW2 (e.g., Chau et al., 2015; Siddiqui et al., 2018).

A large number of studies that have reported the impact of SSWs on the ionosphere have mostly focused on the variability at equatorial and low-latitudes (e.g., Chau et al., 2012; Yiğit & Medvedev, 2015, and references therein). In particular, most of these studies discussed the ionospheric impacts over different longitudinal sectors (e.g., Chau et al., 2010; Fejer et al., 2010; Goncharenko et al., 2010; Liu et al., 2019; Patra et al., 2014; Xiong et al., 2013; Yadav et al., 2017) during the 2009 SSW event. The January 2009 major NH SSW event occurred in the beginning of solar cycle 24 under extremely quiet solar and geomagnetic conditions and is one of the most prolonged SSW on record (e.g., Manney et al., 2009). Toward the end of solar cycle 24, another

major NH SSW event was recorded under similar quiet solar and geomagnetic activity conditions in the final weeks of December 2018 and in the beginning of January 2019. As the occurrence of SSWs under such favorable conditions is seldom, this event provides us further opportunities to investigate the ionospheric impacts of SSWs. Compared to the investigation of SSW related ionospheric variabilities at equatorial and low-latitudes, the mid-latitude ionospheric variability has not yet been thoroughly investigated. Although evidence of mid-latitude ionospheric variability during SSWs using the TEC data have been reported at different longitudinal sectors in a few studies (e.g., Chen et al., 2016; Goncharenko et al., 2013; Polyakova et al., 2014), the TEC data over the European region, which hosts a dense global navigation satellite system (GNSS) networks, have not been much utilized. The objective of the present study is to investigate the mid-latitude TEC variability over Europe during 2009 and 2019 SSWs. As the TEC variability is driven by geomagnetic and lower atmospheric forcing mechanisms, we investigate the dominant drivers and their respective contributions to TEC changes during both SSW events. For this purpose, we utilize GNSS based TEC observations along with TIE-GCM simulations. The SSW effects are simulated in TIE-GCM by specifying the dynamical fields from the WACCM-X simulations of 2009 and 2019 SSWs at the TIE-GCM lower boundary. Through comparison of TIE-GCM simulations with and without geomagnetic forcing, we isolate the TEC variability associated with geomagnetic forcing during both SSWs. As the lower atmospheric forcing effects on the TEC variability during SSWs is primarily realized through the changes in SW2 and M2 tides, we examine the role of these tidal changes on the mid-latitude TEC perturbations through comparison of TIE-GCM simulations performed with and without the SW2 and M2 tides during both these events.

The structure of this paper is as follows. In Section 2, the descriptions of the models and the experiment settings used in this study are provided. The information about the data sets is mentioned in Section 3. The results are presented in Section 4 followed by discussion in Section 5. The summary and conclusions from this work are presented at the end.

2. Model Descriptions and Experiment Settings

2.1. WACCM-X

We use Whole Atmosphere Community Climate Model with thermosphere and ionosphere extension (WACCM-X) version 2.0 (Liu et al., 2018), a configuration of the NCAR Community Earth System Model (CESM 2.0; Hurrell et al., 2013) to perform model simulations in this study. WACCM-X extends from the surface to the upper thermosphere with its top boundary, depending on the solar and geomagnetic activity, lying between 500 and 700 km. The vertical resolution of WACCM-X above the stratosphere is one fourth of a scale height, and the horizontal resolution is $1.9^\circ \times 2.5^\circ$ in latitude and longitude, respectively. WACCM-X is built upon the Whole Atmosphere Community Climate Model (WACCM) (Marsh et al., 2013) and Community Atmosphere Model version 4 (Neale et al., 2013). The new version of WACCM-X has a coupled ionosphere and incorporates self-consistent low-mid-latitude ionospheric electrodynamics adapted from the Thermosphere-Ionosphere Electrodynamics General Circulation Model (TIE-GCM). At high-latitudes, WACCM-X uses an empirical electric potential pattern (Heelis et al., 1982), which is parameterized by the 3-h geomagnetic Kp index and an auroral precipitation oval based on the formulation described by Roble and Ridley (1987). More details about the physical processes included in WACCM-X 2.0 can be found in Liu et al. (2018).

WACCM-X provides a comprehensive tool to study the entire atmosphere-ionosphere system. The impact of lower atmospheric forcing on the upper atmospheric variability can be studied using WACCM-X during specific time periods by constraining the tropospheric and stratospheric dynamics to meteorological reanalysis fields. In the present study, we use the specified dynamics (SD) set up in WACCM-X to simulate the SSWs by constraining the winds and temperatures from 0 to 50 km toward the National Aeronautics and Space Administration Modern Era Retrospective Analysis for Research and Applications (MERRA) Version 2 (Gelaro et al., 2017). Using the approach described in Kunz et al. (2011), the WACCM-X model fields are constrained to the MERRA2 meteorological fields at every model time step (i.e., 5 min). The default SD-WACCM-X set up does not include forcing from the M2 tide but we implement it in our simulations based on the method described by Pedatella, Liu, and Richmond (2012) because the M2 forcing becomes an important source of MLT and ionospheric variability during SSWs. Hourly outputs of winds, temperature and geopotential height are obtained for the 2009 and 2019 SSWs through the SD-WACCM-X runs in this study.

Table 1

TIE-GCM Simulations (Left to Right) Experiment Setups and the Representation of Geomagnetic and Lower Atmospheric Forcings in the Model Runs

Experiment setup	Geomagnetic Forcing	Lower atmospheric forcing
S1	On	On
S2	Off	On
S3	Off	On without SW2 + M2

2.2. TIE-GCM

TIE-GCM is a three dimensional, self-consistent numerical model of the coupled thermosphere-ionosphere system that has been developed at the High Altitude Observatory at the National Center for Atmospheric Research (NCAR). The model spans from ~97 km to about 500–700 km depending on the solar cycle activity. In this study, we use TIE-GCM version 2.0 with a horizontal resolution of 2.5° by 2.5° in geographic longitude and latitude and a vertical resolution of 0.25 times the scale height. The input parameters for TIE-GCM include the solar XUV, EUV and FUV spectral fluxes that are defined by the EUVAC model (Richards et al., 1994) using the F10.7 index. The global electric potential due to the wind dynamo is

solved by the self-consistent TIE-GCM ionospheric electrodynamic at low- and mid-latitudes. At high-latitudes, however, the electric potential is prescribed through empirical convection electric field patterns using the Heelis (Heelis et al., 1982) or Weimer (Weimer, 2005) models. TIE-GCM also uses an analytical auroral model to account for high-latitude auroral particle precipitation in the default set up. The upper part of WACCM-X is based on TIE-GCM and it uses this same auroral model.

The effect of lower atmospheric tidal forcing can be specified in TIE-GCM using the tidal perturbations at its lower boundary (LB). The amplitudes and phases of upward propagating atmospheric tides specified at the TIE-GCM LB in the default setup are based on the Global Scale Wave Model (GSWM) (Hagan et al., 1999). The default TIE-GCM LB assumes constant neutral temperature ($T = 181$ K), geopotential height ($Z = 96.37$ km) and zero horizontal winds (e.g., Maute, 2017). For a more realistic LB conditions, TIE-GCM includes the option to specify hourly inputs at its LB from any other source. In this study, we specify the hourly WACCM-X outputs for 2009 and 2019 SSWs at the TIE-GCM LB and carry out three simulations for each of the SSWs in order to isolate the effects of geomagnetic and lower atmospheric forcings on the TEC variability. In the first simulation setup (hereafter referred to as S1), the TIE-GCM forced by WACCM-X is run in its default mode and the obtained day-to-day ionospheric variability from this run includes the effects of both geomagnetic and lower atmospheric forcings. In the second simulation setup (hereafter referred to as S2), we turn-off the geomagnetic forcing and carry out a similar run for both SSWs. The day-to-day ionospheric variability resulting from the second run arises solely from lower atmospheric forcing during both SSWs. The geomagnetic forcing is turned off from the TIE-GCM runs by reducing the hemispheric power from 18 GW in the first setup to 0.1 GW and the cross-polar cap potential from 30 kV in the first setup to 0.1 kV. Additionally, the Heelis convection model and the analytical auroral model have also been turned off in the second setup to remove the magnetospheric energy input. Using S1 and S2, the contribution of geomagnetic forcing to the TEC variability during both SSWs is estimated. We also perform a third TIE-GCM simulation (hereafter referred to as S3) to assess the importance of SW2 and M2 tides to the TEC variability during both SSWs. In S3, we utilize the settings of S2 and additionally remove the SW2 and M2 tides from the WACCM-X input to TIE-GCM LB. Through comparison of S2 and S3, the contribution of these semidiurnal tides to the TEC changes during both SSWs is estimated. The experiment setups used in this study have been summarized in Table 1. We used TIE-GCM instead of WACCM-X to carry out these three simulations because of the former being computationally less expensive than the latter.

The use of simulations to study the ionospheric effects solely due to lower atmospheric forcing have been implemented in some earlier studies. Pedatella and Maute (2015) simulated the ionospheric effects during the 2013 SSW event solely due to lower atmospheric forcing by running the TIME-GCM simulations under constant solar and geomagnetic activity levels. Yamazaki et al. (2014) used a similar method by running the TIE-GCM under constant solar and magnetospheric energy inputs to study the day-to-day variability of the equatorial electrojet due to lower atmospheric forcing. The occurrence of an SSW event during quiet-time ionospheric conditions is a rarity and there have been many SSWs that occur under active geomagnetic conditions, which complicates the separation of SSW driven ionospheric variability. Our method builds upon the techniques that are presented in Pedatella and Maute (2015) and Yamazaki et al. (2014) and provides a tool to separate the geomagnetic and lower atmospheric forcing effects on the ionospheric variability.

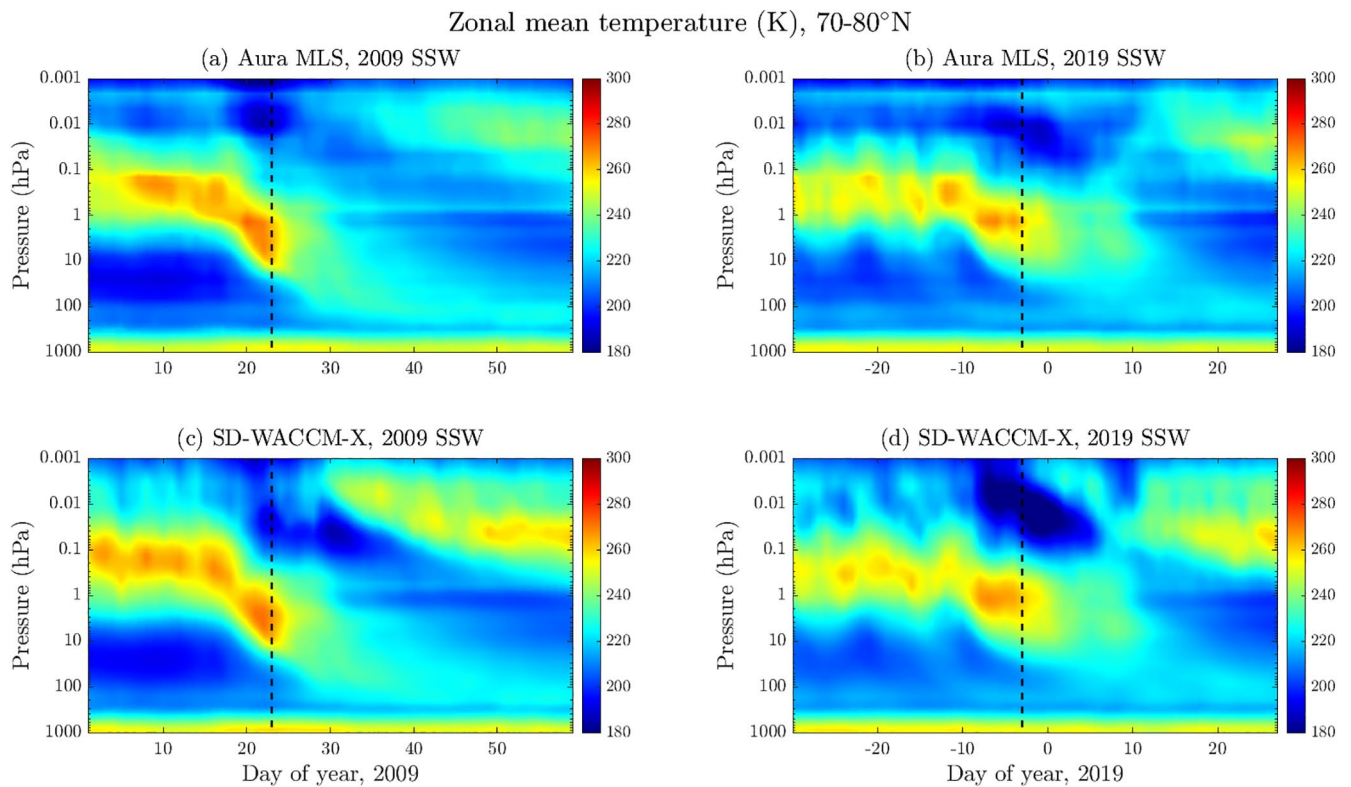


Figure 1. Daily zonal mean temperature (K) averaged between 70° and 80°N as a function of pressure is presented from (a) Aura Microwave Limb Sounder (MLS) observations (c) SD-WACCM-X simulations for the 2009 Sudden Stratospheric Warming (SSW). The same is presented in Figures 1b and 1d, except for the 2019 SSW. The vertical dashed black lines mark the day of polar vortex weakening (PVW) for the corresponding SSWs.

3. Data Sets

For this study, we use the vertical GNSS TEC data during 2009 and 2019 SSWs from the MIT Haystack Observatory's Madrigal database (Rideout & Coster, 2006), which incorporates the data from around 6000 GPS receivers worldwide (Coster et al., 2017). The processed TEC data from the MIT Automated Processing of GNSS (MAPGPS) software provides estimates of TEC over 1° by 1° (latitude by longitude) bins with a temporal resolution of 5 min. The unit of GNSS TEC data is TECu, where 1 TECu is defined as 10^{16} electrons/m².

Hourly values of solar flux ($F_{10.7}$) (Tapping, 2013) have been downloaded from the Space Physics Data facility of the Goddard Space Flight Center through the OMNIWeb data interface to plot the levels of solar activity during the 2009 and 2019 SSWs. The 3-hourly Kp indices are downloaded from the website of German Research Center for Geosciences (GFZ), Potsdam to monitor the geomagnetic activity levels during the two SSW events. We also use the version 5 temperature data from the Microwave Limb Sounder (MLS) onboard the NASA's Earth Observing System (EOS) Aura satellite (Waters et al., 2006) to compare and validate the temperature obtained from WACCM-X simulations.

4. Results

4.1. Zonal Mean and PW Variability During 2009 and 2019 SSWs

In Figure 1, the zonal mean temperatures averaged between 70° and 80°N during January–February 2009 (Figures 1a and 1c) and December 2018–January 2019 (Figures 1b and 1d) from Aura MLS observations (top panels) and SD-WACCM-X simulations (bottom panels) are presented. The vertical dashed black lines in the figure mark the day of polar vortex weakening (PVW). As an alternative to the classical definition of SSW provided by the WMO, PVW has been used to correlate the tidal enhancements in the MLT and ionosphere with the magnitude of the reversal of stratospheric ZMW (e.g., Chau et al., 2015; Siddiqui et al., 2017;

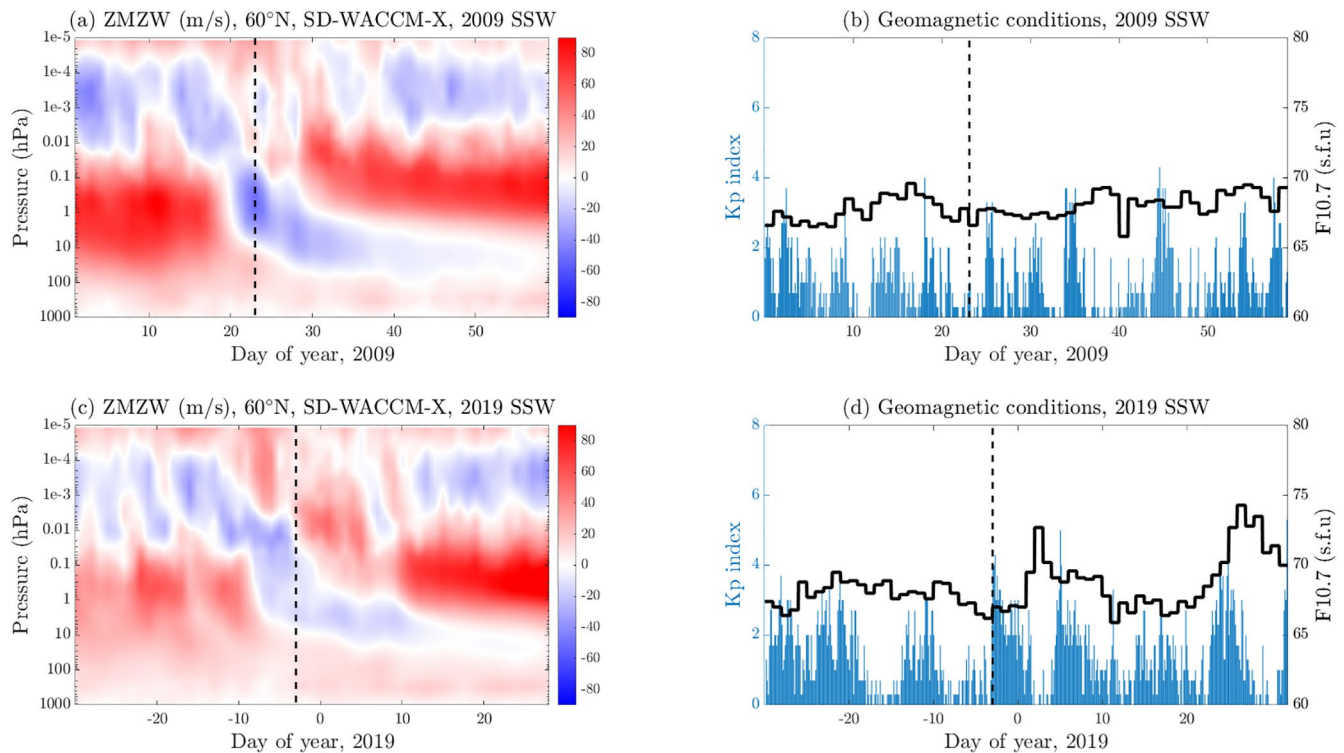


Figure 2. Daily zonal mean zonal wind (ZMW) (m/s) at 60°N as a function of pressure is presented from SD-WACCM-X simulations for (a) 2009 Sudden Stratospheric Warming (SSW) (c) 2019 SSW. The Kp index and solar flux levels are presented for the 2009 SSW in Figure 2b and for the 2019 SSW in Figure 2d. The vertical dashed black lines mark the day of polar vortex weakening (PVW) for the corresponding SSWs.

Zhang & Forbes, 2014). A PVW day is identified by locating the earliest and most extreme reversal of ZMW at 70°N and 48 km altitude (1 hPa) that occurs simultaneously with the increase in zonal mean temperature at North Pole and 40 km altitude (3 hPa) between December and February.

It can be seen that there is a reasonable agreement between the observed and simulated zonal mean temperatures during the considered time intervals. With the onset of each of the SSWs, the warm stratopause descends from its climatological position near 60 km (0.2 hPa) toward lower altitudes, which results in warming at these heights (e.g., Labitzke, 1981) and later breaks down completely in the peak stages of the SSW. The stratopause then reappears at a higher altitude before slowly returning to its original position. This altitudinal shift and reemergence of the stratopause is called an elevated stratopause event and is often associated with major SSW events (e.g., Manney et al., 2008; Siskind et al., 2007). In WACCM-X simulations, the elevated stratopause events are being reproduced for both SSWs but their appearances tend to occur slightly earlier in comparison with the Aura MLS observations. The PVW date for the 2009 SSW event occurs on day 23 (Jan 23) and for the 2019 SSW event on day -3 (Dec 28). The warming of the stratosphere is accompanied by cooling in the mesosphere for both these events. In case of the 2009 SSW, mesospheric cooling can be observed to start around day 20 above 0.1 hPa in Figure 1a and in case of the 2019 SSW around day -8 in Figure 1b. The model temperature simulations are able to reproduce these features to a large extent and are overall consistent with the Aura MLS observations but some discrepancies can also be seen especially at altitudes where SD-WACCM-X stops being constrained to MERRA2, that is, above 50 km (~1 hPa). The differences between SD-WACCM-X and Aura MLS observations start to become apparent above this altitude and are more pronounced in the MLT region. These temperature differences could be related to gravity wave forcing, which is parameterized in SD-WACCM-X and may be contributing to the discrepancy between the observations and model simulations (e.g., Smith, 2012).

The left panels of Figure 2 present the ZMW at 60°N from SD-WACCM-X for the time intervals that include the 2009 and 2019 SSWs while the right panels show the Kp index and daily solar flux (s.f.u) conditions during these SSWs. The dashed black lines show the PVW days in all the panels. For the 2009 SSW, the ZMW

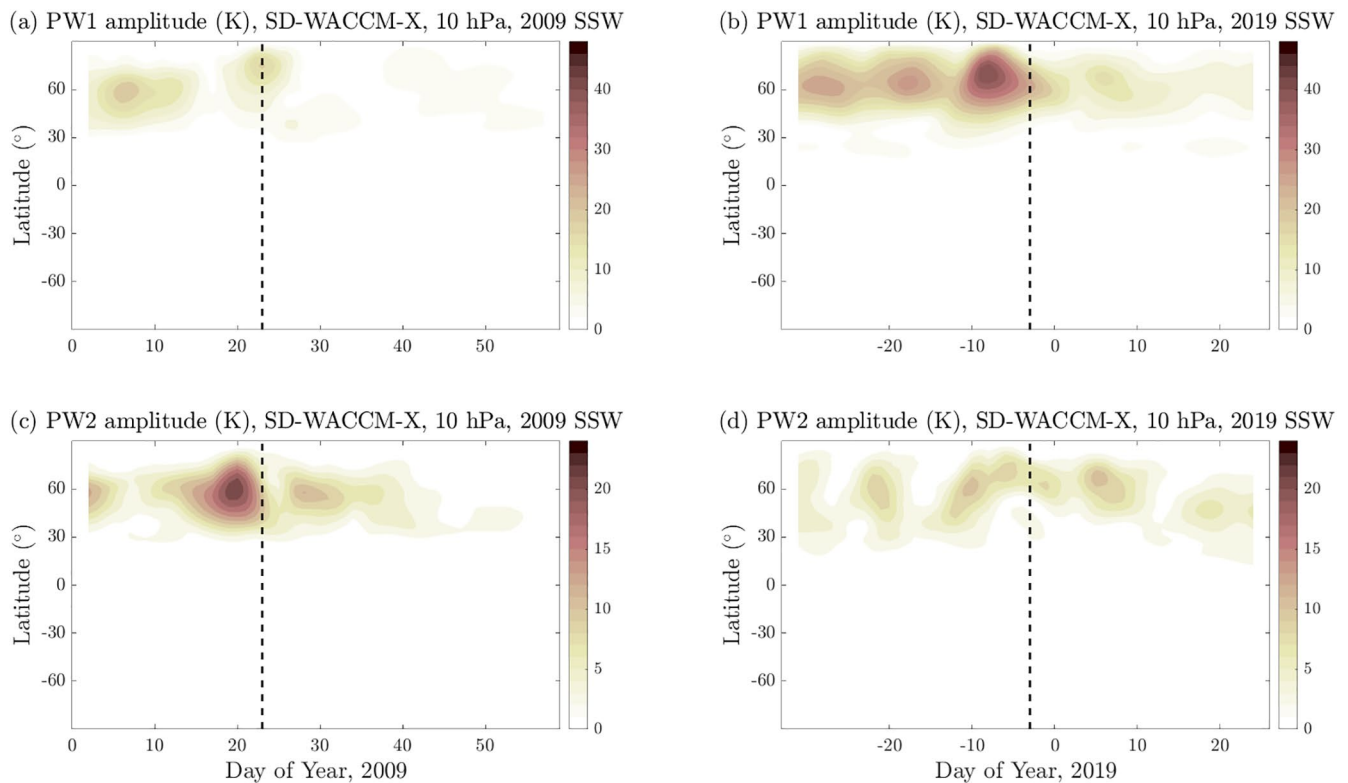


Figure 3. Planetary wave 1 amplitude of temperature at 10 hPa (~30 km) from SD-WACCM-X simulations for (a) 2009 Sudden Stratospheric Warming (SSW) (b) 2019 SSW. The same is presented for planetary wave 2 for (c) 2009 SSW and (d) 2019 SSW. The vertical dashed black lines mark the day of polar vortex weakening (PVW) for the corresponding SSWs.

between 1 and 10 hPa in the stratosphere changes from eastward to westward direction starting around day 20 in Figure 2a. At 10 hPa, the ZMW remains in the reversed direction until day 54 while at 1 hPa, where the PVW is defined, the ZMW reaches a peak reversal on day 23 with a value of about -52 m/s. For the 2019 SSW, the reversal of the ZMW between 1 and 10 hPa is seen toward the end of December around day -8 in Figure 2c. The westward direction of ZMW at 10 hPa remains till day 21 while at 1 hPa, the ZMW is found to reach a peak reversal on day -3 with a value of -15 m/s. From the comparison of the ZMW in Figures 2a and 2c, it can be clearly seen that the 2009 SSW event was stronger in terms of ZMW reversal and more prolonged than the 2019 SSW event.

From the Kp indices and solar flux values in Figures 2b and 2d, it can be inferred that both the 2009 and 2019 SSWs were recorded under periods of relatively low solar and geomagnetic activities. The solar flux levels during 2009 and 2019 SSWs remained below 75 s. f.u for both the events. The geomagnetic activity during the onset and peak phase of the 2009 SSW hovered mostly around $Kp \leq 2+$ with an exception on day 19 when Kp values reached 4o during the 3-hourly intervals. The 2019 SSW event showed higher geomagnetic activity levels as compared to the 2009 SSW event with brief periods of spike in Kp values that reached up to 4+ on day -3 (Dec 28) and 5o on day 5 but overall the period during the 2019 SSW remained geomagnetically quiet.

Figure 3 presents the variability of PWs with wave number 1 (PW1) and 2 (PW2) at 10 hPa in temperature from SD-WACCM-X for the 2009 and 2019 SSWs. In this figure, the colorbar scales of PW1 are chosen to be twice as large in magnitude as compared to those for PW2. The dashed black lines show the PVW days in all the panels. In Figures 3a and 3c, the amplitudes of PW1 and PW2, respectively, are presented for the 2009 SSW event. The enhancement of PW1 is seen in NH high-latitudes particularly around 60°N with peaks on days 6 and 23 while in the case of PW2, the enhancement begins in the second week of January and peaks on day 19. Based on the enhanced amplitudes of PW2 in Figure 3c, we find that our results are consistent with earlier studies (e.g., Manney et al., 2009) that have classified the 2009 SSW as PW2 forced split SSW

event. The amplitudes of PW1 and PW2 for the 2009 SSW are also similar to the results shown using four different whole atmosphere models by Pedatella et al. (2014).

The amplitude of PW1 and PW2 in temperature are presented in Figures 3b and 3d, respectively, for the 2019 SSW event. The PW1 amplitudes show enhancement poleward of 60°N during December with a maximum on day −7. The peak PW1 amplitudes for this event are almost twice as large as compared to that of peak PW1 for the 2009 SSW. The PW2 amplitudes are smaller in magnitude as compared to that of PW1 for this event but enhancement in PW2 is also seen poleward of 60°N toward the end of December with a maxima centered on day −9. The 2019 SSW has been classified in literature as neither a typical displaced nor a typical split SSW event (Rao et al., 2019) but rather a mixed type event, which was initially a displaced SSW and later became a split SSW. From Figure 3b, it can be inferred by the dominance of PW1 amplitudes that the 2019 SSW must have started as a displaced SSW event.

4.2. Migrating Semidiurnal Tides During 2009 and 2019 SSWs

It is well established now that the primary reason for the variability in the ionosphere during SSWs is due to the modulation of atmospheric tides. In particular, the variability of SW2 and M2 tides based on modeling and observational studies have been found to be the most significant driver of ionospheric variabilities (e.g., Chau et al., 2009; Fejer et al., 2010; Forbes & Zhang, 2012; Goncharenko et al., 2012; Lin et al., 2013; Pedatella & Forbes, 2010; Pedatella et al., 2014; Siddiqui et al., 2018; Vineeth et al., 2009; Yamazaki et al., 2012). Atmospheric tides refer to planetary-scale oscillations of the atmosphere that are mainly excited by gravitational forces of the moon and by thermal forcing from the sun (e.g., Forbes & Garrett, 1978; Forbes, 1982; Lindzen & Chapman, 1969). These oscillations have periods and sub-periods of a solar or a lunar day. The solar tides form the dominating component of the tidal oscillations and are predominantly thermally forced. The excitation mechanisms include daily periodic absorption of solar energy by tropospheric water vapor and stratospheric ozone (e.g., Forbes & Wu, 2006; Zhang et al., 2010) while the relatively smaller lunar tides are mainly forced due to the lunar gravitational effects on the Earth's atmosphere. In this section, we investigate the variability of the SW2 and M2 tides during both SSW events.

The hourly outputs of neutral temperature from SD-WACCM-X simulations are used to extract the components of the solar and lunar tides by performing a least squares fit with a moving window of 15 days at each latitude. The following equation based on Pedatella, Liu, and Richmond (2012) has been used to make the fit:

$$\sum_{n=0}^3 \sum_{s=n-5}^{n+5} A_{n,s} \cos(n\Omega t + s\lambda - \phi_{n,s}) + \sum_{s=-3}^3 L_s \cos(2\tau + (s-2)\lambda - \Phi_s) \quad (1)$$

where $\Omega = \frac{2\pi}{24}$ hour⁻¹, t is universal time in hours, n denotes the harmonics of a solar day, λ is the longitude, s is the zonal wave number, $A_{n,s}$ and $\phi_{n,s}$ are the amplitude and phase of the solar tidal components. For a wave propagating westward $s > 0$, while for a wave propagating eastward $s < 0$. L_s and Φ_s represent the amplitude and the phase of the semidiurnal lunar tide, respectively.

Figure 4 presents the amplitudes of the SW2 (top panels) and M2 (bottom panels) tides in neutral temperature at 1×10^{-4} hPa (~110 km altitude) from SD-WACCM-X simulations for the 2009 and 2019 SSWs. The vertical dashed black lines mark the days of PVW for each of these SSWs. In Figure 4a, the SW2 tidal variability for the 2009 SSW shows enhanced amplitudes of ~21 K at SH mid-latitudes on day 15 and amplitudes >25 K starting around day 35. In the NH, the SW2 enhancements are only seen after day 25 and enhanced amplitudes of ~24 K are found from simulations. Following the PVW day, there is a sudden decrease in the amplitude of SW2 at SH mid-latitudes. This feature of SW2 was also reported in a study by Pedatella et al. (2014) where they compared the temporal variability of SW2 during the 2009 SSW event using four different whole atmosphere models. Figure 4c presents the amplitude of M2 tide where we notice its enhancement to ~10 K in both hemispheres a few days after the PVW day. Another enhancement of M2 reaching ~9 K is seen in the NH after day 40. The M2 variability from SD-WACCM-X during this SSW event is consistent with the results of Zhang and Forbes (2014). They also reported similar M2 enhancements using neutral temperature measurements at 110 km altitude from the Sounding of the Atmosphere using Broadband Emission Radiometry (SABER) instrument onboard the Thermosphere Ionosphere Mesosphere Energetics Dynamics (TIMED) satellite. Figures 4b and 4d shows the amplitudes of SW2 and M2 tides, respectively, in neutral

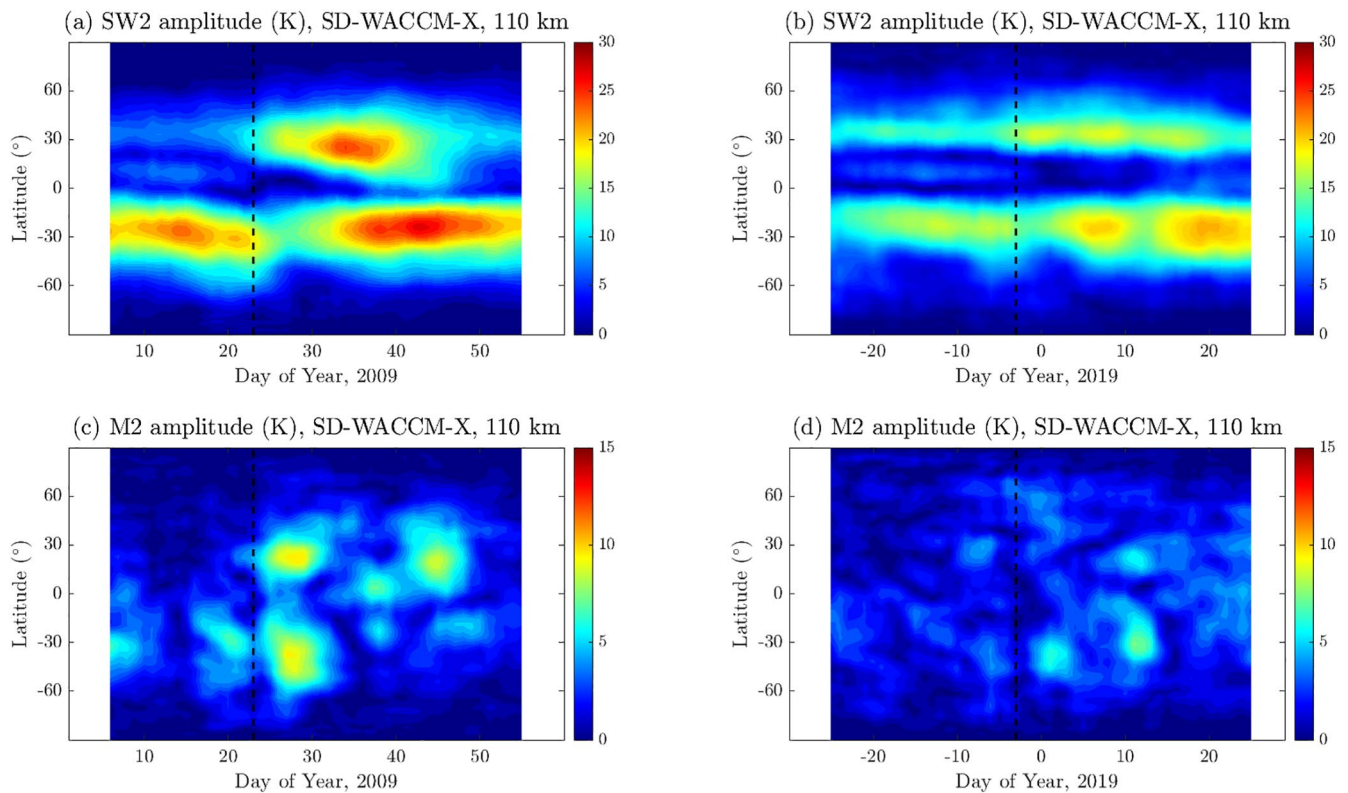


Figure 4. SW2 tidal amplitudes in neutral temperature at 1×10^4 hPa (~ 110 km) from SD-WACCM-X for (a) 2009 Sudden Stratospheric Warming (SSW) and (b) 2019 SSW events. The lunar (M2) tides in neutral temperature at the same altitude is presented in (c and d) for the 2009 and 2019 SSWs, respectively. The vertical dashed black lines mark the day of polar vortex weakening (PVW) for the corresponding SSWs.

temperature between December 2018 and January 2019. Similar to the SW2 variability during the 2009 SSW event, the SW2 amplitude in Figure 4b shows enhancement at SH mid-latitudes on either side of the PVW day with a reduction of SW2 amplitude in between. The SW2 amplitude reaches a peak of ~ 17 K on day -12 and ~ 20 K on day 8 in the SH. In the NH, the SW2 amplification starts close to the PVW day and it reaches a value of ~ 18 K on day 9. In Figure 4d, the first M2 enhancement in SH with peak amplitudes of ~ 6.5 K happens a few days after the PVW day. The second M2 enhancement in the SH with peak amplitude of ~ 7.5 K is seen around day 11. Following Chau et al. (2015) and Conte et al. (2017), we also performed tidal analyses using a 21-day running window (see Supporting Information S1) to further reduce any artifacts or ambiguity between the determination of SW2 and M2 tides but we found the amplification of M2 to be similar to that shown in Figures 4c and 4d. We find that the M2 amplitude during the 2019 SSW is smaller (~ 2.5 K) as compared to that during the 2009 SSW event. One reason for the difference in amplification could be related to the timing of the SSW event relative to the phase of the moon. Pedatella and Liu (2013) have shown from simulation results that the lunar tidal response in the ionosphere is dependent upon the phase of the moon relative to the timing of the SSW event. Further, Fejer et al. (2010) have found that the lunar effects in the ionosphere during SSWs amplify close to the new or the full moon days. The new moon day for the 2009 SSW occurred 3 days after the PVW day while for the 2019 it was recorded 6 days before the PVW. This difference in the timing of the new moon days relative to the PVW days may also be contributing to the reduced amplification of M2 during the 2019 SSW.

4.3. Comparison of Observed and Simulated M2 Variability During 2009 and 2019 SSWs

Figure 5 presents the M2 tidal amplitudes for the 2009 and 2019 SSW events obtained using the V2.0 temperature measurements from the SABER instrument onboard the TIMED satellite at an altitude of 110 km. We employ the least squares fitting method mentioned in Zhang and Forbes (2014) to determine the M2 amplitudes from zonally averaged SABER temperature residuals. As the period of the M2 tide from the

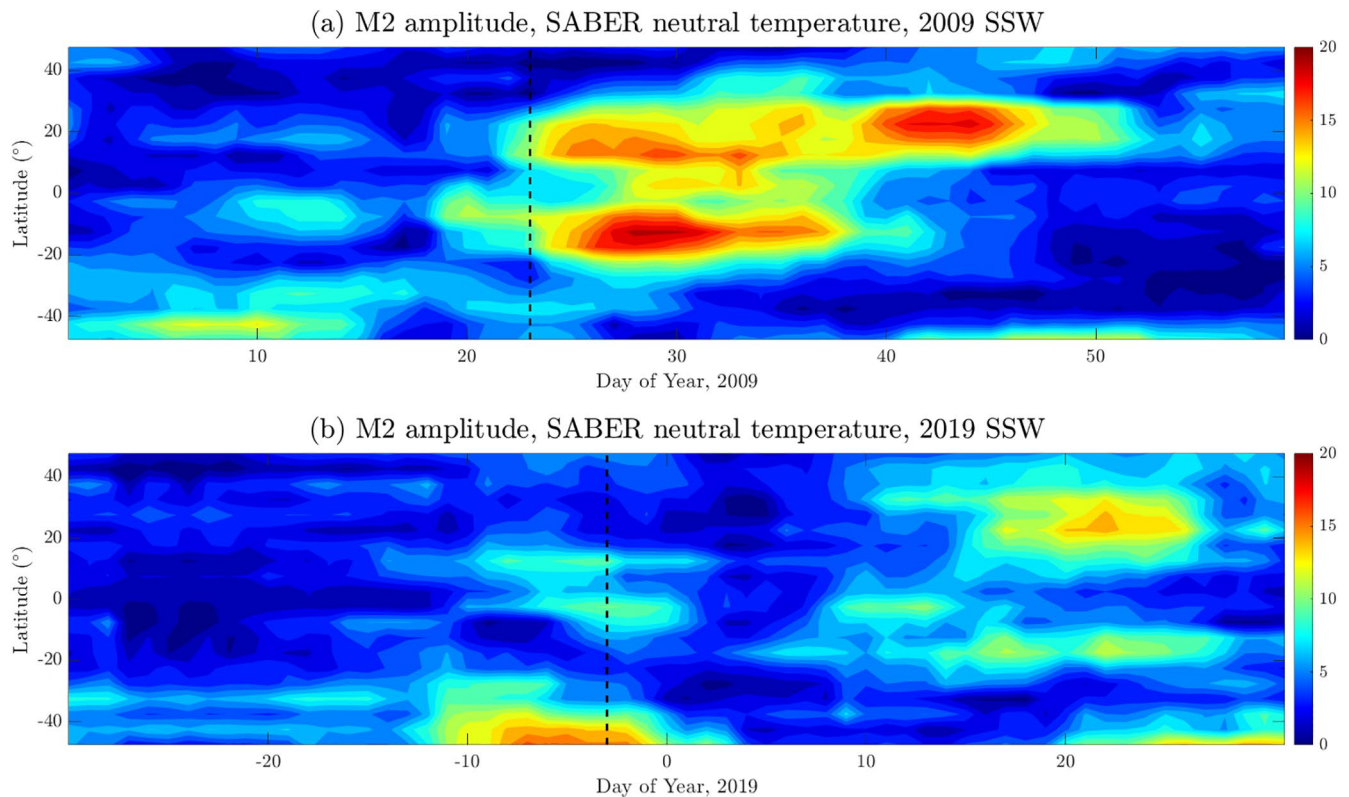


Figure 5. Amplitude of lunar (M2) tide at 110 km from Sounding of the Atmosphere using Broadband Emission Radiometry (SABER) V2.0 temperature measurements for (a) 2009 Sudden Stratospheric Warming (SSW) (b) 2019 SSW. The vertical dashed black lines mark the day of polar vortex weakening (PVW) for the corresponding SSWs.

frame of the TIMED satellite is 11.85 days (Forbes et al., 2013), we use a 12-day moving window and fit only the M2 tide to the daily zonally averaged temperature residuals. Figures 5a and 5b show the amplitude of the M2 tide for the 2009 and 2019 SSWs, respectively. The vertical dashed black lines show the days of PVW. The enhancement of M2 following the PVW can be seen at low- and mid-latitudes for the 2009 SSW event in Figure 5a. This plot of M2 amplitude is similar to the one shown in Zhang and Forbes (2014) (see Figure 1). The M2 tides in neutral temperature from SD-WACCM-X simulations for the 2009 SSW, shown in Figure 4c, match very well with the M2 from SABER temperature observations in terms of the timing of the M2 enhancement. In the NH, the day-to-day variability of the M2 amplitudes from SD-WACCM-X simulations is slightly more consistent with those obtained from SABER temperature observations as the M2 peaks are located at similar latitudes. In the SH, the M2 peaks from SABER observations on day 27 are slightly more equatorward as compared to those from SD-WACCM-X simulations. The M2 amplitudes for the 2019 SSW presented in Figure 5b shows that the level of M2 enhancement for this SSW was clearly lower than that for the 2009 SSW. The M2 enhancements can be seen to occur toward the end of December 2018 between days -7 and 0 poleward of 40°S and around day 22 above 20°N . The enhancement in the SH toward the end of December is also captured in M2 from SD-WACCM-X simulations in Figure 4d. But the M2 amplitudes from SD-WACCM-X do not exactly reproduce the observations for the 2019 SSW event as the M2 peak around day 22 in the NH is not seen in the simulations. There is similarity between the observed and simulated M2 amplitudes in the sense that the enhancements were particularly weaker for the 2019 SSW as compared to the 2009 SSW event, which is confirmed from both the simulated and observed M2 amplitudes in the simulations. There is similarity between the observed and simulated M2 amplitudes in the sense that the enhancements were particularly weaker for the 2019 SSW as compared to the 2009 SSW event, which is confirmed from both the simulated and observed M2 amplitudes.

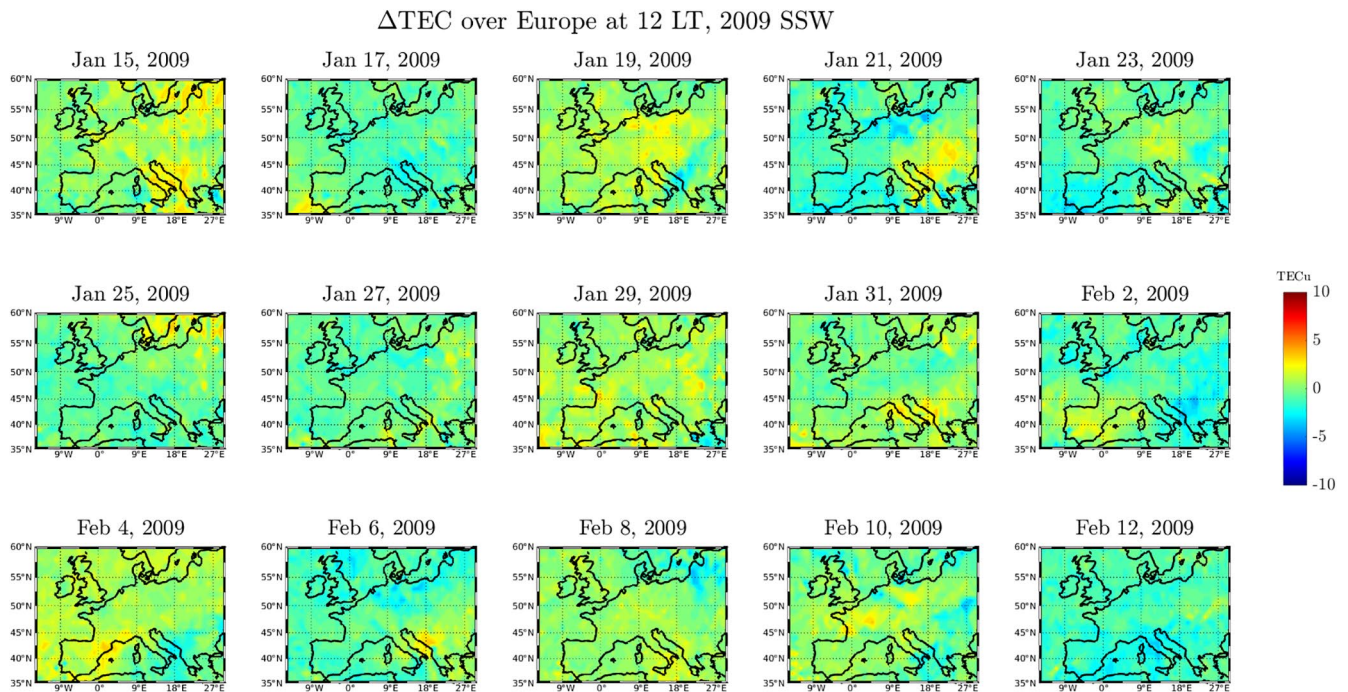


Figure 6. Total Electron Content (TEC) perturbations (Δ TEC) over Europe from global navigation satellite system (GNSS) TEC observations at 12 LT between January 15, 2009 and February 12, 2009.

4.4. GNSS TEC Variability Over Europe During 2009 and 2019 SSWs

In this section of the paper, we analyze the variability of GNSS based TEC over Europe during the 2009 and 2019 SSWs. We compute the hourly TEC data between 35°N and 60°N geographic latitudes and 15°W–30°E, in the European sector by taking the mean vertical TEC values within ± 30 min for each local time (LT). The standard deviation for each hourly bin lies typically between 0 and 1.5 TECu. In order to examine the SSW associated TEC perturbations, we first determine the hourly quiet background TEC using median values from a 27-day moving window that is centered on a given day. The 27-day median TEC (TEC_{median}) has been used as an effective method to estimate the quiet background TEC for comparison against disturbances (e.g., Borries et al., 2015; Mendillo, 2006). The perturbations in TEC, Δ TEC, are then calculated during the 2009 and 2019 SSW events by using,

$$\Delta TEC = TEC - TEC_{median} \quad (2)$$

The typical uncertainties in the 27-day median values, estimated using the median of absolute deviations (MAD) (Müller, 2000) comes out to be between 0.5 and 1 TECu.

We looked at the TEC variability over Europe for all the LTs during the 2009 and 2019 SSWs and found that the maximum variability is observed at around 12 LT. In Figures 6 and 7, we therefore present Δ TEC (in TECu) observed at 12 LT over Europe for 2009 and 2019 SSWs. For both these events, we cover the pre-, peak-, and post-SSW periods. Δ TEC is presented on alternate days between January 15, 2009 and February 12, 2009 for the 2009 SSW. For the 2019 SSW, Δ TEC is similarly presented between December 18, 2018 and January 15, 2019. In Figure 6, Δ TEC for the 2009 SSW event shows minor changes at European latitudes with magnitudes remaining less than 4 TECu over the entire period. Compared to Δ TEC at low-latitudes, where magnitudes of more than 10 TECu were observed in the American sector at similar LTs during the 2009 SSW (e.g., Goncharenko et al., 2010), the Δ TEC values at mid-latitudes are relatively minor in absolute terms. In Figure 7, Δ TEC for the 2019 SSW is presented. In the pre-SSW period, Δ TEC values are < 3 TECu but on December 28, 2018, during the peak SSW phase, a relatively large enhancement is observed in Δ TEC, which covers the majority of European latitudes. In the South-West parts of Europe, Δ TEC values reach ~ 10 TECu on this day. A reduction in Δ TEC values by ~ 4 TECu is seen on January 3, 2019 between 35°N and 40°N that is followed by an enhancement of a similar amount between 40°N and 50°N on January 5, 2019.

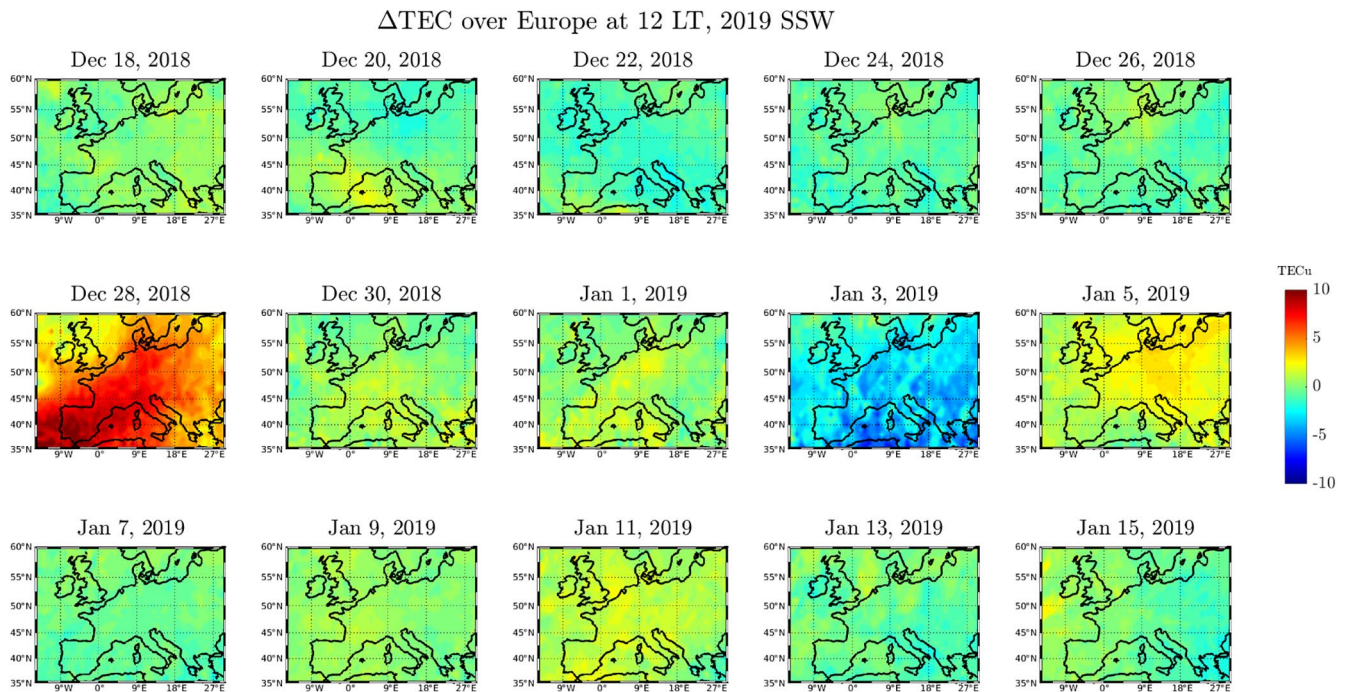


Figure 7. Total Electron Content (TEC) perturbations (Δ TEC) over Europe from global navigation satellite system (GNSS) TEC observations at 12 LT between December 18, 2018 and January 15, 2019.

The Δ TEC magnitudes during the 2019 SSW event in Figure 7 are clearly stronger than for the 2009 SSW event in Figure 6.

It is to be noted that the timing of Δ TEC enhancement on December 28, 2018 for the 2019 SSW event coincides with its PVW day. Moreover, from Figure 2d we have seen that the daytime Kp values increased to 40 on this day. The enhancement in Δ TEC could therefore be a result of processes involving both geomagnetic and lower atmospheric forcings. The individual contribution of both these mechanisms to the Δ TEC enhancements needs to be ascertained in order to quantify their relative importance for the respective SSW events. We investigate the Δ TEC enhancement in more detail in the next section with TIE-GCM simulations to find the dominant forcing mechanism that caused the observed TEC variability over Europe.

5. Discussion

5.1. Comparison Between Observed and Simulated TEC During 2009 and 2019 SSWs

Based on the GNSS TEC observations in Figure 7, it seems that the TEC variability over Europe during the 2019 SSW may also be affected by moderately enhanced geomagnetic activity levels as noted by the increase in Kp values. To identify the main driver for this TEC variability, we isolate the individual contributions of geomagnetic and lower atmospheric forcings to TEC variability using TIE-GCM simulations. Additionally, in order to check the veracity of the simulated TEC from TIE-GCM simulations during SSWs, we performed a comparison with the observed low-latitude TEC variations that was reported by Goncharenko et al. (2010) over the American sector during the 2009 SSW (see Supporting Information S2). We see the characteristic semi-diurnal signature in simulated TEC around the central day of 2009 SSW over the American sector that was reported by Goncharenko et al. (2010). As the TIE-GCM simulations are able to qualitatively reproduce the TEC observations at low-latitudes during the 2009 SSW, it gives us the confidence that they can also be used to study the mid-latitude TEC variability during SSWs.

In this section, we first present the observed GNSS TEC results in Figures 8a and 9a before comparing it with the simulated TEC from three different TIE-GCM setups. The readers may note that there has been a change in the sequential order with the 2019 SSW event being presented prior to the 2009 SSW event in

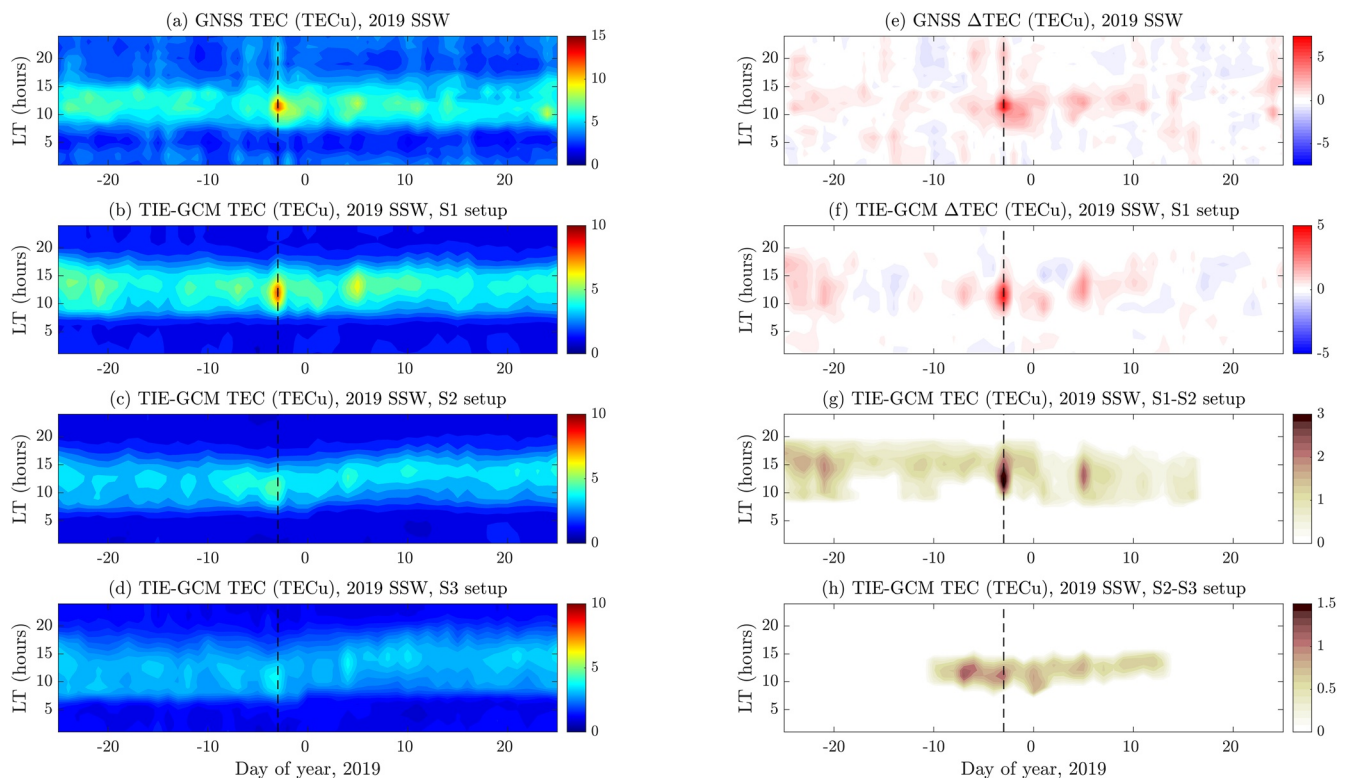


Figure 8. (a) Daily averaged global navigation satellite system (GNSS) Total Electron Content (TEC) over Europe as a function of local time for the 2019 Sudden Stratospheric Warming (SSW). The TIE-GCM simulated TEC is presented in the same format for (b) S1, (c) S2, and (d) S3 setups. TEC perturbations (Δ TEC) over Europe from (e) GNSS TEC observations and (f) TIE-GCM simulations as a function of local time for the 2019 SSW. The TEC difference from S1 and S2 setups is plotted in (g) and the TEC difference from S2 and S3 setups is plotted in (h). The filled contour lines in (g) and (h) are only plotted when absolute TEC difference exceeds 0.25 TECu. The vertical dashed black lines mark the day of polar vortex weakening (PVW).

order to facilitate the topical discussion. In Figure 8a, we take the averaged value of GNSS TEC over the European region shown in Figure 7 for each LT and present the temporal evolution of averaged TEC (Figure 8a) and Δ TEC (Figure 8e) as a function of local time for the 2019 SSW. The dashed black lines mark the PVW day. The diurnal variation of TEC is evident in Figure 8a with the TEC values increasing gradually in the morning hours before reaching a maximum in the afternoon hours and then declining gradually post sunset. The day-to-day variability of TEC, which is subject to solar, geomagnetic and lower atmospheric forcings, can also be seen in Figure 8a. The TEC enhancements reach values of ~ 12.5 TECu at 12 LT on day -3 and ~ 8.5 TECu at 12 LT on day 5. Δ TEC in Figure 8e is calculated using Equation 2 as before and shows the perturbations of TEC from the quiet background TEC values. The spike in both averaged TEC and Δ TEC values on days -3 (Dec 28) and 5 (Jan 5) between 10 and 12 LT can also be seen in this figure, with Δ TEC reaching ~ 6 TECu on day -3 and to ~ 2.5 TECu on day 5 at 12 LT.

Figure 8b shows the average of the simulated TEC over Europe for the S1 run. We note that the TEC derived from TIE-GCM simulations are able to reproduce the TEC spikes on days -3 (Dec 28) and 5 (Jan 5) and are qualitatively similar in comparison to the averaged GNSS TEC in Figure 8a. The modeled and observed TEC may only be compared in a qualitative sense owing to the upper boundary limit of TIE-GCM, which depending on the solar activity extends only up to 500–700 km in altitude, thus hindering a quantitative comparison with GNSS TEC observations. The modeled TEC results demonstrate that the TIE-GCM simulation includes the various forcing mechanisms that are responsible for the observed TEC variability in Figure 8a and can be used to filter out contributions of the mid-latitude sources of TEC variability. The averaged TEC enhancements over Europe reach values of ~ 8.5 TECu at 12 LT on day -3 and ~ 6.5 TECu at 13 LT on day 5. From the simulated Δ TEC in Figure 8f, we can see that the TEC spikes on day -3 at 12 LT reach ~ 4 TECu and on day 5 to ~ 2 TECu at 12 LT.

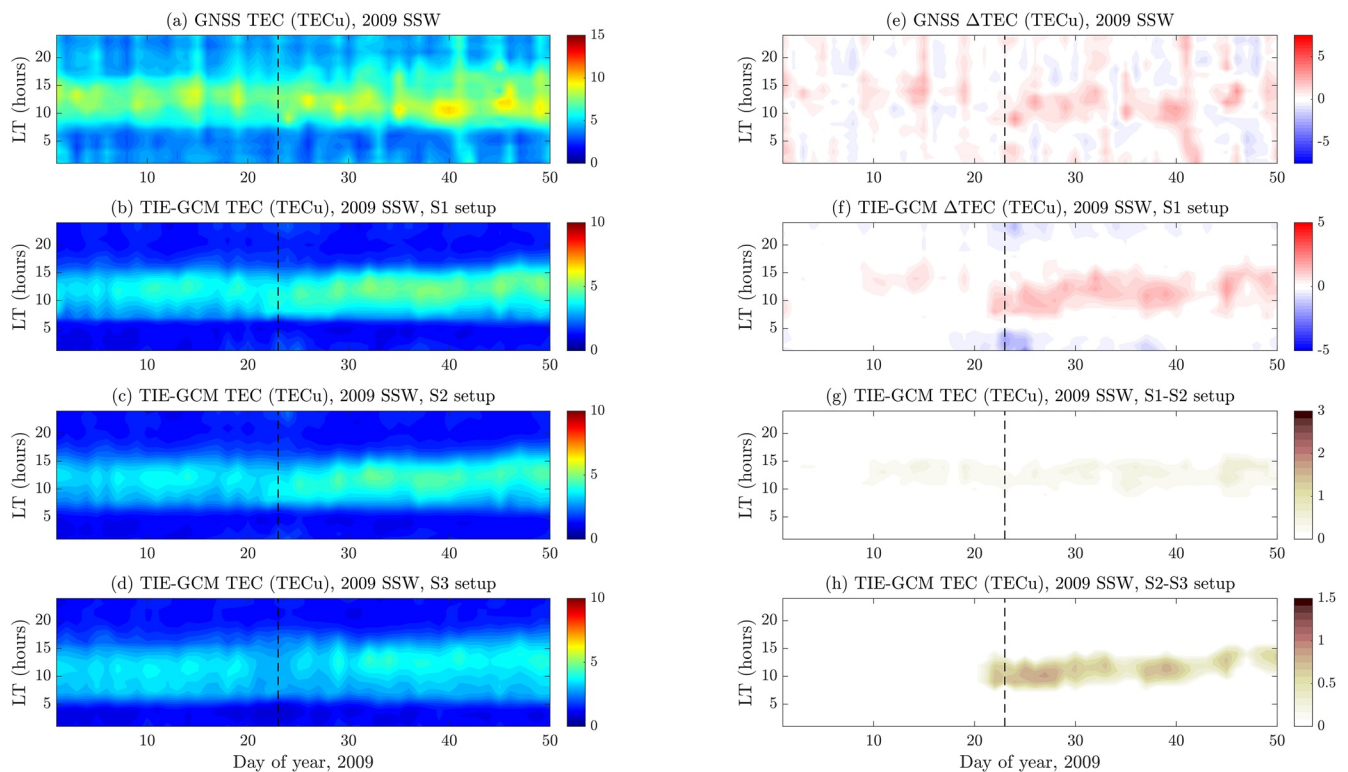


Figure 9. Same as Figure 8 except for the 2009 Sudden Stratospheric Warming (SSW).

In Figure 8c, the averaged TEC over Europe is presented for the S2 run. It can be noticed that there is an apparent reduction of the averaged TEC values after turning off geomagnetic forcing and the peak TEC values have been reduced to less than 5 TECu. The major TEC enhancements in this plot can be seen on days -3 and 4 with peak TEC values reaching ~ 5 and ~ 4.5 TECu, respectively, between 10 and 14 LT. In Figure 8d, the averaged TEC over Europe is presented for the S3 run. For this setup, the averaged TEC over Europe shows further reduction in the TEC peaks and on days -3 and 4 it reduces to the level of background TEC values between 10 and 14 LT, which suggests that the contribution of SW2 and M2 tides to the TEC variability for this SSW is not negligible and therefore needs to be assessed in more detail.

In Figure 8g, the difference of TEC values from S1 and S2 setups ($TEC_{S1-S2} = TEC_{S1} - TEC_{S2}$), is presented. The filled contour lines are plotted when absolute value of TEC_{S1-S2} exceeds 0.25 TECu. It can be clearly noted that the major difference is seen on days -3 and 5 when peak TEC_{S1-S2} values between 12 and 14 LT reach ~ 3 and ~ 2 TECu, respectively. Compared to the simulated background TEC values of ~ 4 TECu at 12 LT, we find that the geomagnetic forcing is responsible for increasing the background TEC values by $\sim 75\%$ on day -3 (Dec 28) and by $\sim 50\%$ on day 5 (Jan 5) at 12 LT. It can therefore be easily inferred that the major processes causing the TEC spikes on days -3 and 5 between 10 and 14 LT are related to geomagnetic forcing. In Figure 8h, the difference of TEC values from S2 and S3 setups ($TEC_{S2-S3} = TEC_{S2} - TEC_{S3}$), is presented. Through this plot, the contribution of the SW2 and M2 tides to TEC variability can be assessed. The SW2 and M2 tides have been used in the analysis as they have been reported to be a major source of ionospheric variability during an SSW event (e.g., Fejer et al., 2010; Goncharenko et al., 2010; Jin et al., 2012; Pedatella et al., 2012). The filled contour lines are again plotted when absolute value of TEC_{S2-S3} exceeds 0.25 TECu. We find that the TEC variability due to SW2 and M2 tides start close to the SSW onset on day -10 and continues up to day 12. The SW2 and M2 tidal changes associated with the 2019 SSW seem to modulate the daytime electric field through the E-region dynamo process, which results in the TEC variability as seen in this figure. The SW2 and M2 tides increase the background TEC values by approximately ~ 1 – 1.5 TECu, which corresponds to $\sim 20\%$ – 25% increase in the background TEC.

The individual contributions of the geomagnetic and lower atmospheric forcings on the TEC variability over Europe is also similarly assessed for the 2009 SSW event. In Figure 9a, the averaged GNSS TEC over Europe as a function of local time is presented for the 2009 SSW event. In addition to the diurnal and day-to-day variability of TEC, major TEC enhancements are observed in Figure 9a between 10 and 12 LT on days 40 and 45. In Figure 9e, ΔTEC shows the perturbations of TEC from the quiet median TEC values. Here, large TEC perturbations particularly on days 40 and 45 are clearly noticeable with ΔTEC being ~ 2 TECu between 10 and 13 LT. The averaged TEC derived from the TIE-GCM run with S1 setup is presented in Figure 9b. A qualitative comparison with GNSS TEC observations in Figure 9a suggests that the primary features of the averaged TEC variability are similar in the simulations. The comparatively lower levels of averaged TEC before day 30 between 10 and 15 LT and the moderately enhanced averaged TEC levels after this day have been correctly reproduced in the simulation. The simulated TEC enhancements on days 40 and 45 at 13 LT are smaller in comparison to observed TEC. We present the ΔTEC from TIE-GCM simulations in Figure 9f. Compared to the GNSS ΔTEC , we find that the TEC enhancements on days 40 and 45 between 10 and 14 LT are smaller in the simulated ΔTEC with values reaching ~ 1 TECu.

In Figures 9c and 9d, the averaged TEC over Europe from TIE-GCM runs with S2 and S3 setups are presented. We notice that there is a decrease in TEC values when the geomagnetic forcing has been turned off but we also find that most of the features of the averaged TEC from S1 setup have been reproduced in the averaged TEC from S2 setup, which suggests that the lower atmospheric forcing processes are the dominant drivers of TEC variability during the 2009 SSW event. We calculate the difference of TEC values from S1 and S2 setups (TEC_{S1-S2}) in Figure 9g and plot the filled contour lines when absolute values of TEC_{S1-S2} exceed 0.25 TECu. We find that the TEC variability solely due to geomagnetic forcing lies mostly below 0.25 TECu in this period and exceeds this limit noticeably only on day 45 between 12 and 14 LT. In Figure 9h, the difference of TEC values from S2 and S3 setups, TEC_{S2-S3} , is presented. As seen earlier for the case of 2019 SSW, the contribution of SW2 and M2 tides to TEC variability can be assessed through this plot. The filled contour lines are plotted when TEC_{S2-S3} exceeds 0.25 TECu. The TEC variability due to SW2 and M2 tides starts around day 20 when the onset of the 2009 SSW event occurs and continues onward till day 50. The TEC variability reaches ~ 1 TECu at 10 LT between days 23 and 28 and at 11 LT around day 40 before dropping to ~ 0.75 TECu at 13 LT around day 45. For the 2009 SSW event, the SW2 and M2 tides are responsible for $\sim 20\%$ – 25% increase in the background TEC, which is similar to the levels seen during the 2019 SSW event.

5.2. Possible Reasons for the Observed TEC Variability

Most of the studies that documented the ionospheric effects of SSWs, especially during the 2009 SSW, focused on the variability at equatorial and low-latitudes (e.g., Chau et al., 2012; Yiğit & Medvedev, 2015, and references therein). While it is now accepted that the mechanisms causing the variability at these latitudes are driven by the changes in the vertically propagating semidiurnal solar and lunar tides, the mechanisms responsible for the mid-latitude ionospheric variability during SSWs are not as well understood. Simulation results by Pedatella and Maute (2015) have shown that the variability of the mid-latitude ionospheric F-region peak height (hmF2) during SSWs is predominantly driven by the field-aligned neutral winds, which is modulated by the M2 tidal enhancements. Yue et al. (2010) observed the global ionospheric response using Constellation Observing System for Meteorology, Ionosphere, and Climate (COSMIC) satellites during the 2009 SSW and suggested the changes in the neutral wind and composition due to direct propagation of tides as another mechanism for the ionospheric mid-latitude variability during SSWs. It is also known from observations and modeling studies that the influence of SSWs at mid- and high-latitudes ionosphere is generally smaller as compared to that at low-latitudes. Oyama et al. (2014) used the FORMOSAT-3/COSMIC peak ionospheric electron density (NmF2) data and found that changes in mid-latitude NmF2 to be only between 20% and 30% during the 2009 SSW, which was comparably lower than the changes at low-latitudes. Their observation results were found to be consistent with the simulations shown by Pedatella and Maute (2015). For the 2009 and 2019 SSW events, our results also show similar numbers as the background TEC values over Europe increase by $\sim 20\%$ – 25% due to SSW associated SW2 and M2 tidal changes. The amplification of SW2 and M2 tides in the peak SSW phase were relatively larger for the 2009 SSW in comparison with the 2019 SSW but their contributions to the TEC variability, in terms of TEC enhancement, remain similar. However, the SW2+M2 contribution to TEC variability lasts for a week longer during the 2009 SSW event as compared to the 2019 SSW event. For the 2019 SSW, the SW2+M2 influence on the TEC variability are seen

TEC & TECP over Europe, December 28, 2018

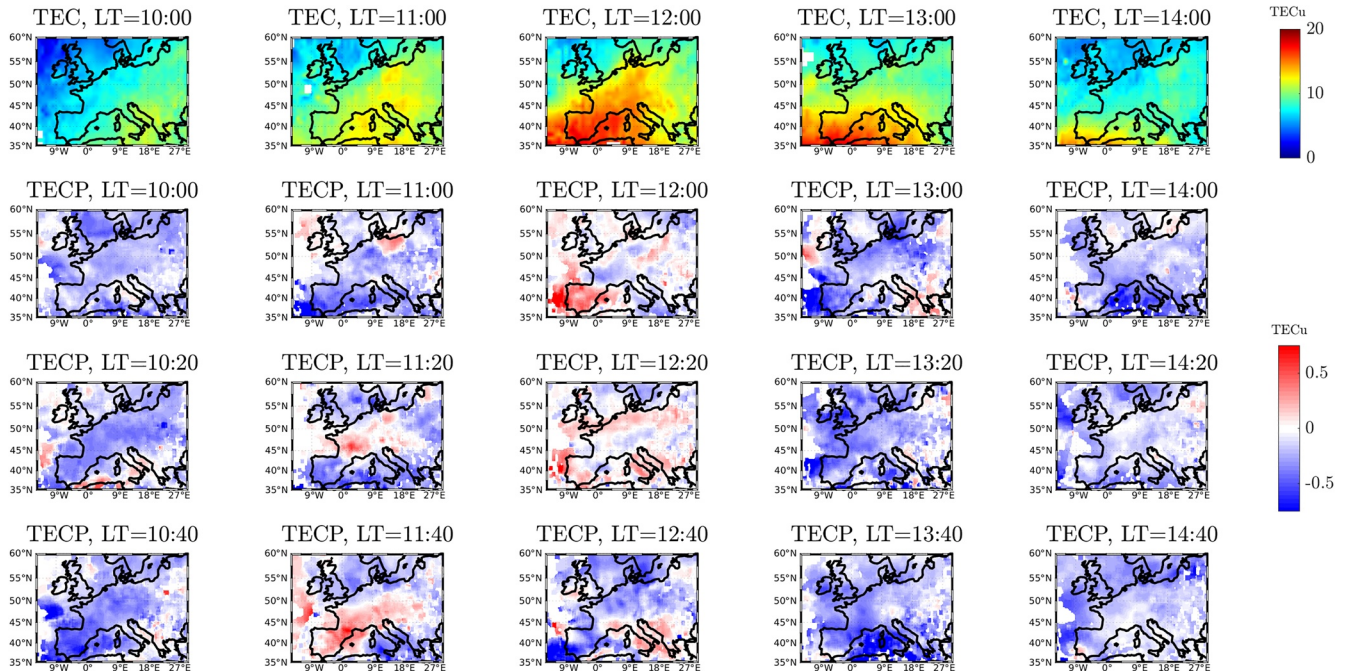


Figure 10. Global navigation satellite system (GNSS) Total Electron Content (TEC) and TECP values over Europe on December 28, 2019. The TEC values are presented between 10 and 14 LT in the top panels at an interval of every 1 h. The TECP values are presented in the lower panels between 10:00 and 14:40 LT at an interval of every 20 min.

between days -10 and 10 (~ 3 weeks) and for the 2009 SSW between days 20 and 50 (~ 4 weeks). This could be a result of a second M2 enhancement seen around day 45 for the 2009 SSW event, which contributes to a longer influence of SW2+M2 on TEC for this SSW.

During the 2019 SSW event, along with the increase in Kp values to 4+ on December 28, the meridional component of the interplanetary magnetic field (IMF) in Geocentric Solar Magnetospheric (GSM) coordinate system, B_z turned southward and reached down to -7.5 nT, and the Auroral Electrojet (AE) index reached to $\sim 1,100$ nT. The symmetric disturbance field in H (SYM-H) index declined from 26 nT on December 27 to -30 nT on December 28. Based on the statistical measures, the geomagnetic activity parameters resemble the conditions of a weak geomagnetic storm (e.g., Yokoyama & Kamide, 1997). From the results in Figure 8, it is clear that the sudden surge in daytime TEC observations over Europe on December 28 is due to geomagnetic forcing. To explore the mechanisms behind the daytime TEC enhancement on this day, we present hourly GNSS TEC maps over Europe between 10 and 14 LT constructed with a resolution of 30 min in the top panels of Figure 10. The TEC values are seen to increase across Europe after 10 LT and reach a maxima at 12 LT before declining at later hours. An equatorward movement in the TEC can be observed between 12 and 14 LT, which suggests that these TEC fluctuations could be due to large-scale traveling ionospheric disturbances (LSTIDs). LSTIDs are ionospheric fluctuations associated with traveling atmospheric disturbances (TADs), which are generated in the auroral region when the polar ionosphere is subjected to energy input from the magnetosphere (e.g., Prölss, 1995). As the TADs propagate to middle- and low-latitudes, they induce perturbations in the neutral wind, which can lead to the upward/downward movement of plasma along the magnetic field lines leading to ionospheric fluctuations commonly known as LSTIDs (e.g., Lei et al., 2008). The propagation direction of LSTIDs is usually in the equatorward direction and they have a horizontal scale of $>1,000$ km and a period between 30 min and 3 h (e.g., Hunsucker, 1982). GNSS TEC maps are an excellent tool to identify the structure and temporal evolution of LSTIDs (e.g., Tsugawa et al., 2004). LSTIDs can be detected by detrending the observed TEC data with a 1 h running mean to retrieve the perturbation component of TEC (TECP) (e.g., Tsugawa et al., 2004). Below the top panels in Figure 10, we present sequence of TECP maps at an interval of every 20 min starting from 10 LT. It is possible

to recognize the LSTID signatures in the TECP maps after 11 LT with the crest of LSTID starting around 55° N and 10°E and propagating in the equatorward direction. This crest continues to progress equatorward at later times and when it reaches ~40°N at 12:20 LT, a second crest appears at ~50°N. The LSTID signatures moved below 35°N after 13 LT. The LSTID features seen in Figure 10 is consistent with the earlier observations of LSTIDs made over Europe (e.g., Zakharenkova et al., 2016). Therefore, we believe that major contribution to the TEC enhancement on December 28, 2018 could be caused by geomagnetic storm associated LSTIDs.

Along with LSTIDs, the increase in TEC over Europe could also be contributed by positive storm effect mechanism. During geomagnetic storms, the relative increase in the ionospheric plasma density with respect to quiet-time conditions is referred to as positive storm effect (e.g., Astafyeva et al., 2016; Goncharenko et al., 2007; Matsushita, 1959). The storm-time increase in TEC in Figure 10 can result from several competing physical processes that are mainly driven by variations in electric fields of different origins and changes in thermospheric neutral winds composition and circulation. During geomagnetic disturbances, electric fields of magnetospheric origin map to high-latitude ionosphere along the geomagnetic field lines and generate various disturbance electric fields that include prompt-penetration electric field (PPEF) (e.g., Kelley et al., 1979), disturbance dynamo electric field (DDEF) (Blanc & Richmond, 1980) and the subauroral polarization stream (SAPS) electric field (e.g., Foster & Burke, 2002). The effects of these electric fields along with the mechanical effects of the thermospheric wind (Balan et al., 2010) are responsible for the redistribution of ionospheric plasma during a geomagnetic storm and could be contributing to the TEC enhancements seen over Europe.

It has also been observed that minor geomagnetic storms can cause anomalous positive storm effects on the mid-latitude ionosphere under extremely low solar activity conditions that are comparable with the effects of strong geomagnetic storms occurring under higher solar activity conditions (e.g., Buresova et al., 2014; Cander & Haralambous, 2011; Sunda et al., 2013). In the study by Buresova et al. (2014) it was observed that under low solar activity conditions between 2007 and 2009, the changes in F2 layer critical frequency (fof2) could reach up to 100% as compared to its 27-day running mean at mid-latitude stations during minor geomagnetic disturbances. In a recent study by Rajesh et al. (2020), extreme and unexpected TEC enhancements were observed globally during a weak geomagnetic storm on August 5, 2019. Their results showed that despite of Kp values remaining at about 5+, the TEC values over the European region on August 05 almost tripled with respect to the reference value on the pre-storm day (see Figures 4 and 5 of Rajesh et al. (2020)). They reported that the mid-latitude TEC enhancements over Europe on August 05, 2019 seems to be unrelated to the PPEF driven enhanced equatorial fountain but appears to result from the plasma accumulation associated with the storm-induced equatorward surge of neutral winds. This hypothesis is supported in our results from the observations of equatorial propagating LSTIDs. The mechanisms behind this unexpected and intense positive storm effect feature at mid-latitudes should be investigated further in more detail. However, understanding the role of each mechanism behind the positive storm effect feature at mid-latitudes remain the most unpredictable feature of geomagnetic storms and is beyond the scope of the current study at present.

6. Conclusions

The variability in the mid-latitude TEC over Europe was investigated during 2009 and 2019 SSWs in the present study using GNSS TEC observations and TIE-GCM simulations. The 2019 SSW period was accompanied by weak geomagnetic storm-like conditions and the main feature of the observed TEC response during this SSW was a positive spike in the daytime TEC that coincided with its PVW day. In comparison, the TEC response during the 2009 SSW period showed only mild day-to-day variations over European mid-latitudes. The TIE-GCM simulations reproduce the observed TEC variations during both SSWs and have therefore been used to isolate the individual contribution of geomagnetic and lower atmospheric forcings to the TEC variability during both SSWs. Through comparison of TIE-GCM simulations with and without geomagnetic forcing, we find that the dominant TEC enhancement during the 2019 SSW were geomagnetically forced while for the 2009 SSW, the TEC enhancement was mainly due to lower atmospheric forcing. We also examined the importance of SW2 and M2 tides on the TEC variability at mid-latitudes during both SSWs and

found their role to be minor in comparison to that at low-latitudes. Based on the results we summarize our findings as follows:

1. It is found that the spike in TEC over Europe during the 2019 SSW was geomagnetically forced and may be a result of LSTIDs. Geomagnetic forcing accounts for about ~75% of the TEC variability during the 2019 SSW while the remaining is accounted for by lower atmospheric forcing.
2. In contrast, the variability of TEC over Europe during the 2009 SSW was predominantly due to lower atmospheric forcing. The minor TEC increase were mostly due to the SSW induced tidal changes in SW2 and M2.
3. The SW2 and M2 tides increase the background TEC values by ~20%–25% during both SSWs, which is similar to the levels reported by previous observation and modeling based studies.

Although simulation results have shown that the SSW associated effects increase the background TEC by ~20%–25% at European mid-latitudes, it is difficult to distinguish these effects from quiet-time day-to-day variability using TEC maps alone. Compared to the TEC perturbations at low-latitudes in the American sector (e.g., Goncharenko et al., 2010), the TEC perturbations at European mid-latitudes is found to be appreciably lower due to SSWs.

Data Availability Statement

The geomagnetic activity index Kp was provided by the GFZ German Research Centre for Geosciences (<https://www.gfz-potsdam.de/en/kp-index/>). The solar activity index F10.7 was downloaded from the SPDF OMNIWeb database (<https://omniweb.gsfc.nasa.gov>). The ground-based GNSS TEC data are available through the MIT Haystack Observatory Madrigal database (<http://madrigal.haystack.mit.edu/madrigal/>). Data for the TEC processing is provided from the following organizations: UNAVCO, Scripps Orbit and Permanent Array Center, Institut Geographique National, France, International GNSS Service, The Crustal Dynamics Data Information System (CDDIS), National Geodetic Survey, Instituto Brasileiro de Geografia e Estatística, RAMSAC CORS of Instituto Geográfico Nacional de la República Argentina, Arecibo Observatory, Low-Latitude Ionospheric Sensor Network (LISN), Topcon Positioning Systems, Inc., Canadian High Arctic Ionospheric Network, Institute of Geology and Geophysics, Chinese Academy of Sciences, China Meteorology Administration, Centro di Ricerche Sismologiche, Système d'Observation du Niveau des Eaux Littorales (SONEL), RENAG: REseau NATIONAL GPS permanent, GeoNet - the official source of geological hazard information for New Zealand, GNSS Reference Networks, Finnish Meteorological Institute, SWE-POS - Sweden, Hartebeesthoek Radio Astronomy Observatory, Crustal Dynamics Data Information System (CDDIS), Astronomical Institute of the University of Bern, TrigNet Web Application, South Africa, Australian Space Weather Services, RETE INTEGRATA NAZIONALE GPS, Estonian Land Board, and Virginia Tech Center for Space Science and Engineering Research. The neutral temperature obtained from WACCM-X simulation for the 2009 SSW event have been publicly made available and uploaded through the Mendeley data set with the following link (<http://dx.doi.org/10.17632/47pnw8pgmk.1>). For the 2019 SSW, it can be found with the following link (<http://dx.doi.org/10.17632/48257xrmx3.1>).

Acknowledgments

GNSS TEC data products and access through the Madrigal distributed data system are provided to the community by the Massachusetts Institute of Technology under support from US National Science Foundation grant AGS-1762141. The authors thank the Aura/MLS team and NASA/JPL for the microwave limb sounding measurements and the availability of the level2 data set at the Aura Validation Data Center (<http://avdc.gsfc.nasa.gov/>). T. A. Siddiqui and M. Sivakandan acknowledge support from Humboldt research Fellowship for Postdoctoral Researchers. This material is based upon work supported by the National Center for Atmospheric Research, which is a major facility sponsored by the National Science Foundation under Cooperative Agreement No. 1852977. This work was supported in part by the European Space Agency through Contract 4000126709/19/NL/IS "VERA." The authors also thank Nick Pedatella for providing helpful comments and suggestions on an earlier draft of the manuscript. Open Access funding enabled and organized by Projekt DEAL.

References

- Allen, D. R., Bevilacqua, R. M., Nedoluha, G. E., Randall, C. E., & Manney, G. L. (2003). Unusual stratospheric transport and mixing during the 2002 Antarctic winter. *Geophysical Research Letters*, 30(12). <https://doi.org/10.1029/2003GL017117>
- Andrews, D. G., Holton, J. R., & Leovy, C. B. (1987). *Middle atmosphere dynamics* (No. 40). Academic press.
- Astafyeva, E., Zakharenkova, I., & Pineau, Y. (2016). Occurrence of the dayside three-peak density structure in the F2 and the topside ionosphere. *Journal of Geophysical Research: Space Physics*, 121(7), 6936–6949. <https://doi.org/10.1002/2016JA022641>
- Baker, W., & Martyn, D. F. (1953). Electric currents in the ionosphere—the conductivity. *Philosophical Transactions of the Royal Society of London*, 246(913), 281–294. <https://doi.org/10.1098/rsta.1953.0016>
- Balan, N., Shiokawa, K., Otsuka, Y., Kikuchi, T., Vijaya Lekshmi, D., Kawamura, S., et al. (2010). A physical mechanism of positive ionospheric storms at low latitudes and midlatitudes. *Journal of Geophysical Research*, 115(A2). <https://doi.org/10.1029/2009JA014515>
- Baldwin, M. (2003). Major stratospheric warming in the Southern Hemisphere in 2002: Dynamical aspects of the ozone hole split. *SPARC newsletter*, 20, 24–26.
- Blanc, M., & Richmond, A. (1980). The ionospheric disturbance dynamo. *Journal of Geophysical Research*, 85(A4), 1669–1686. <https://doi.org/10.1029/JA085iA04p01669>
- Borries, C., Berdermann, J., Jakowski, N., & Wilken, V. (2015). Ionospheric storms - A challenge for empirical forecast of the total electron content. *Journal of Geophysical Research: Space Physics*, 120(4), 3175–3186. <https://doi.org/10.1002/2015JA020988>

- Buresova, D., Laštovička, J., Hejda, P., & Bochnicek, J. (2014). Ionospheric disturbances under low solar activity conditions. *Advances in Space Research*, 254(2), 185–196. <https://doi.org/10.1016/j.asr.2014.04.007>
- Butler, A. H., Seidel, D. J., Hardiman, S. C., Butchart, N., Birner, T., & Match, A. (2015). Defining sudden stratospheric warmings. 96. 1913–1928. *Bulletin of the American Meteorological Society*. <https://doi.org/10.1175/BAMS-D-13-00173.1>
- Cander, L. R., & Haralambous, H. (2011). On the importance of the total electron content enhancements during the extreme solar minimum. *Advances in Space Research*, 47(2), 304–311. <https://doi.org/10.1016/j.asr.2010.08.026>
- Chandran, A., & Collins, R. (2014). Stratospheric sudden warming effects on winds and temperature in the middle atmosphere at middle and low latitudes: A study using WACCM. *Annales Geophysicae*, 32(7), 32–874. <https://doi.org/10.5194/angeo-32-859-2014>
- Charlton, A. J., & Polvani, L. M. (2007). A new look at stratospheric sudden warmings. Part I: Climatology and modeling benchmarks. *Journal of Climate*, 20(3), 449–469. <https://doi.org/10.1175/JCLI3996.1>
- Charney, J. G., & Drazin, P. G. (1961). Propagation of planetary-scale disturbances from the lower into the upper atmosphere. *Journal of Geophysical Research*, 66(1), 83–109. <https://doi.org/10.1029/JZ0661001p00083>
- Chau, J. L., Aponte, N. A., Cabassa, E., Sulzer, M. P., Goncharenko, L. P., & González, S. A. (2010). Quiet time ionospheric variability over Arecibo during sudden stratospheric warming events. *Journal of Geophysical Research*, 115(A9), A00G06. <https://doi.org/10.1029/2010JA015378>
- Chau, J. L., Fejer, B. G., & Goncharenko, L. P. (2009). Quiet variability of equatorial ExB drifts during a sudden stratospheric warming event. *Geophysical Research Letters*, 36(5). <https://doi.org/10.1029/2008GL036785>
- Chau, J. L., Goncharenko, L. P., Fejer, B. G., & Liu, H.-L. (2012). Equatorial and low latitude ionospheric effects during sudden stratospheric warming events. *Space Science Reviews*, 168(1), 385–417. <https://doi.org/10.1007/s11214-011-9797-5.01>
- Chau, J. L., Hoffmann, P., Pedatella, N. M., Matthias, V., & Stober, G. (2015). Upper mesospheric lunar tides over middle and high latitudes during sudden stratospheric warming events. *Journal of Geophysical Research: Space Physics*, 120, 3084–3096. <https://doi.org/10.1002/2015JA020998>
- Chen, G., Wu, C., Zhang, S., Ning, B., Huang, X., Zhong, D., et al. (2016). Midlatitude ionospheric responses to the 2013 SSW under high solar activity. *Journal of Geophysical Research: Space Physics*, 121(1), 790–803. <https://doi.org/10.1002/2015JA021980>
- Conte, J. F., Chau, J. L., Stober, G., Pedatella, N., Maute, A., Hoffmann, P., et al. (2017). Climatology of semidiurnal lunar and solar tides at middle and high latitudes: Interhemispheric comparison. *Journal of Geophysical Research: Space Physics*, 122(7), 7750–7760. <https://doi.org/10.1002/2017ja024396>
- Coster, A. J., Goncharenko, L., Zhang, S.-R., Erickson, P. J., Rideout, W., & Vierinen, J. (2017). GNSS observations of ionospheric variations during the 21 August 2017 solar eclipse. *Geophysical Research Letters*, 44(24). <https://doi.org/10.1002/2017GL075774>
- Eswaraiah, S., Kim, Y. H., Liu, H., Ratnam, M. V., & Lee, J. (2017). Do minor sudden stratospheric warmings in the Southern Hemisphere (SH) impact coupling between stratosphere and mesosphere–lower thermosphere (MLT) like major warmings? *Earth Planets and Space*, 69(1), 119. <https://doi.org/10.1186/s40623-017-0704-5>
- Fejer, B. G., Olson, M. E., Chau, J. L., Stolle, C., Lühr, H., Goncharenko, L. P., et al. (2010). Lunar-dependent equatorial ionospheric electrodynamic effects during sudden stratospheric warmings. *Journal of Geophysical Research*, 115(A8), A00G03. <https://doi.org/10.1029/2010JA015273>
- Forbes, J. M. (1982). Atmospheric tides: 1. Model description and results for the solar diurnal component. *Journal of Geophysical Research: Space Physics*, 87(A7), 5222–5240. <https://doi.org/10.1029/JA087A07p05222>
- Forbes, J. M., & Garrett, H. B. (1978). Thermal excitation of atmospheric tides due to insolation absorption by O₃ and H₂O. *Geophysical Research Letters*, 5(12), 1013–1016. <https://doi.org/10.1029/GL005i012p01013>
- Forbes, J. M., & Wu, D. (2006). Solar tides as revealed by measurements of mesosphere temperature by the MLS experiment on UARS. *Journal of the Atmospheric Sciences*, 63(7), 1776–1797. <https://doi.org/10.1175/JAS3724.1>
- Forbes, J. M., & Zhang, X. (2012). Lunar tide amplification during the January 2009 stratosphere warming event: Observations and theory. *Journal of Geophysical Research*, 117(A12), 117. <https://doi.org/10.1029/2012JA017963>
- Forbes, J. M., Zhang, X., Bruinsma, S., & Oberheide, J. (2013). Lunar semidiurnal tide in the thermosphere under solar minimum conditions. *Journal of Geophysical Research: Space Physics*, 118(4), 1788–1801. <https://doi.org/10.1029/2012ja017962>
- Foster, J., & Burke, W. (2002). SAPS: A new categorization for sub-auroral electric fields. *Eos, Transactions American Geophysical Union*, 83(36), 393–394. <https://doi.org/10.1029/2002eo000289>
- Fritz, S., & Soules, S. (1970). Large-scale temperature changes in the stratosphere observed from Nimbus III. *Journal of the Atmospheric Sciences*, 27(7), 1091–1097. [https://doi.org/10.1175/1520-0469\(1970\)027<1091:lstcit>2.0.co;2](https://doi.org/10.1175/1520-0469(1970)027<1091:lstcit>2.0.co;2)
- Funke, B., López-Puertas, M., Bermejo-Pantaleón, D., García-Comas, M., Stiller, G. P., von Clarmann, T., et al. (2010). Evidence for dynamical coupling from the lower atmosphere to the thermosphere during a major stratospheric warming. *Geophysical Research Letters*, 37(13), L13803. <https://doi.org/10.1029/2010GL043619>
- García, R. R. (1987). On the mean meridional circulation of the middle atmosphere. *Journal of the Atmospheric Sciences*, 44(24), 3599–3609. [https://doi.org/10.1175/1520-0469\(1987\)044<3599:otmmco>2.0.co;2](https://doi.org/10.1175/1520-0469(1987)044<3599:otmmco>2.0.co;2)
- Gelaro, R., McCarty, W., Suárez, M. J., Todling, R., Molod, A., Takacs, L., et al. (2017). The Modern-Era Retrospective Analysis for Research and Applications, Version 2 (MERRA-2). *Journal of Climate*, 30(14), 5419–5454. <https://doi.org/10.1175/JCLI-D-16-0758.1>
- Goncharenko, L., Chau, J. L., Condor, P., Coster, A., & Benkevitch, L. (2013). Ionospheric effects of sudden stratospheric warming during moderate-to-high solar activity: Case study of January 2013. *Geophysical Research Letters*, 40(19), 4982–4986. <https://doi.org/10.1002/grl.50980>
- Goncharenko, L. P., Chau, J. L., Liu, H.-L., & Coster, A. J. (2010). Unexpected connections between the stratosphere and ionosphere. *Geophysical Research Letters*, 37(10). <https://doi.org/10.1029/2010GL043125>
- Goncharenko, L. P., Coster, A. J., Chau, J. L., & Valladares, C. E. (2010). Impact of sudden stratospheric warmings on equatorial ionization anomaly. *Journal of Geophysical Research: Space Physics*, 115(A10). <https://doi.org/10.1029/2010JA015400>
- Goncharenko, L. P., Coster, A. J., Plumb, R. A., & Domeisen, D. I. V. (2012). The potential role of stratospheric ozone in the stratosphere-ionosphere coupling during stratospheric warmings. *Geophysical Research Letters*, 39(8). <https://doi.org/10.1029/2012GL051261>
- Goncharenko, L. P., Foster, J., Coster, A. J., Cheryl, H. (2007). Observations of a positive storm phase on September 10, 2005. *Journal of Atmospheric and Solar*, 69(10), 1253–1272. <https://doi.org/10.1016/j.jastp.2006.09.011>
- Goncharenko, L. P., & Zhang, S.-R. (2008). Ionospheric signatures of sudden stratospheric warming: Ion temperature at middle latitude. *Geophysical Research Letters*, 35(21). <https://doi.org/10.1029/2008GL035684>
- Hagan, M. E., Burrage, M. D., Forbes, J. M., Hackney, J., Randel, W. J., & Zhang, X. (1999). GSWM-98: Results for migrating solar tides. *Journal of Geophysical Research*, 104(A4), 6813–6827. <https://doi.org/10.1029/1998JA900125>

- Heelis, R. A., Lowell, J. K., & Spiro, R. W. (1982). A model of the high-latitude ionospheric convection pattern. *Journal of Geophysical Research*, 87(A8), 6339–6345. <https://doi.org/10.1029/JA087iA08p06339>
- Hunsucker, R. D. (1982). Atmospheric gravity waves generated in the high-latitude ionosphere: A review. *Reviews of Geophysics*, 20(2), 293–315. <https://doi.org/10.1029/RG020i002p00293>
- Hurrell, J. W., Holland, M. M., Gent, P. R., Ghan, S., Kay, J. E., Kushner, P. J., & Marshall, S. (2013). The community earth system model: A framework for collaborative research. *Bulletin of the American Meteorological Society*, 94(9), 1339–1360. <https://doi.org/10.1175/BAMS-D-12-00121.1>
- Jin, H., Miyoshi, Y., Pancheva, D., Mukhtarov, P., Fujiwara, H., & Shinagawa, H. (2012). Response of migrating tides to the stratospheric sudden warming in 2009 and their effects on the ionosphere studied by a whole atmosphere-ionosphere model GAIA with COSMIC and TIMED/SABER observations. *Journal of Geophysical Research*, 117(A10). <https://doi.org/10.1029/2012JA017650>
- Karlsson, B., McLandress, C., & Shepherd, T. G. (2009). Inter-hemispheric mesospheric coupling in a comprehensive middle atmosphere model. *Journal of Atmospheric and Solar*, 71(3–4), 518–530. <https://doi.org/10.1016/j.jastp.2008.08.006>
- Kelley, M. C., Fejer, B. G., & Gonzales, C. A. (1979). An explanation for anomalous equatorial ionospheric electric fields associated with a northward turning of the interplanetary magnetic field. *Geophysical Research Letters*, 6(4), 301–304. <https://doi.org/10.1029/GL006i004p00301>
- Körnich, H., & Becker, E. (2010). A simple model for the interhemispheric coupling of the middle atmosphere circulation. *Advances in Space Research*, 45(5), 661–668. <https://doi.org/10.1016/j.asr.2009.11.001>
- Kunz, A., Pan, L. L., Konopka, P., Kinnison, D. E., & Tilmes, S. (2011). Chemical and dynamical discontinuity at the extratropical tropopause based on START08 and WACCM analyses. *Journal of Geophysical Research*, 116(D24). <https://doi.org/10.1029/2011JD016686>
- Labitzke, K. (1972). Temperature changes in the mesosphere and stratosphere connected with circulation changes in winter. *Journal of the Atmospheric Sciences*, 29(4), 756–766. [https://doi.org/10.1175/1520-0469\(1972\)029<0756:tcitma>2.0.co;2](https://doi.org/10.1175/1520-0469(1972)029<0756:tcitma>2.0.co;2)
- Labitzke, K. (1981). Stratospheric-mesospheric midwinter disturbances: A summary of observed characteristics. *Journal of Geophysical Research*, 86(C10), 9665–9678. <https://doi.org/10.1029/JC086iC10p09665>
- Lei, J., Burns, A. G., Tsugawa, T., Wang, W., Solomon, S. C., & Wiltberger, M. (2008). Observations and simulations of quasiperiodic ionospheric oscillations and large-scale traveling ionospheric disturbances during the December 2006 geomagnetic storm. *Journal of Geophysical Research*, 113(A6). <https://doi.org/10.1029/2008JA013090>
- Lin, C., Lin, J., Chang, L., Chen, W., Chen, C., & Liu, J. (2013). Stratospheric sudden warming effects on the ionospheric migrating tides during 2008–2010 observed by FORMOSAT-3/COSMIC. *Journal of Atmospheric and Solar-Terrestrial Physics*, 103, 66–75. <https://doi.org/10.1016/j.jastp.2013.03.026>
- Lindzen, R. S., & Chapman, S. (1969). Atmospheric tides. *Space Science Reviews*, 10(1), 3–188. <https://doi.org/10.1007/bf00171584>
- Liu, H.-L., Bardeen, C. G., Foster, B. T., Lauritzen, P., Liu, J., & Lu, G. (2018). Development and validation of the whole atmosphere community climate model with thermosphere and ionosphere extension (WACCM-X 2.0). *Journal of Advances in Modeling Earth Systems*, 10(2), 381–402. <https://doi.org/10.1002/2017ms001232>
- Liu, H.-L., & Roble, R. G. (2002). A study of a self-generated stratospheric sudden warming and its mesospheric-lower thermospheric impacts using the coupled TIME-GCM/CCM3. *Journal of Geophysical Research*, 107(D23), 4695. <https://doi.org/10.1029/2001JD001533>
- Liu, H.-L., Wang, W., Richmond, A. D., & Roble, R. G. (2010). Ionospheric variability due to planetary waves and tides for solar minimum conditions. *Journal of Geophysical Research*, 115(A6). <https://doi.org/10.1029/2009JA015188>
- Liu, J., Zhang, D.-H., Hao, Y.-Q., & Xiao, Z. (2019). The comparison of lunar tidal characteristics in the low-latitude ionosphere between east Asian and American sectors during stratospheric sudden warming events: 2009–2018. *Journal of Geophysical Research: Space Physics*, 124(8), 7013–7033. <https://doi.org/10.1029/2019JA026722>
- Manney, G. L., Krüger, K., Pawson, S., Minschwaner, K., Schwartz, M. J., Daffer, W. H., & Waters, J. W. (2008). The evolution of the stratopause during the 2006 major warming: Satellite data and assimilated meteorological analyses. *Journal of Geophysical Research*, 113(D11). <https://doi.org/10.1029/2007JD009097>
- Manney, G. L., Schwartz, M. J., Krüger, K., Santee, M. L., Pawson, S., Lee, J. N., & Livesey, N. J. (2009). Aura Microwave Limb Sounder observations of dynamics and transport during the record-breaking 2009 Arctic stratospheric major warming. *Geophysical Research Letters*, 36(12), L12815. <https://doi.org/10.1029/2009GL038586>
- Marsh, D. R., Mills, M. J., Kinnison, D. E., Lamarque, J.-F., Calvo, N., & Polvani, L. M. (2013). Climate change from 1850 to 2005 simulated in CESM1(WACCM). *Journal of Climate*, 26(19), 7372–7391. <https://doi.org/10.1175/JCLI-D-12-00558.1>
- Matsuno, T. (1971). A dynamical model of the stratospheric sudden warming. *Journal of the Atmospheric Sciences*, 28(8), 1479–1494. [https://doi.org/10.1175/1520-0469\(1971\)028<1479:admots>2.0.co;2](https://doi.org/10.1175/1520-0469(1971)028<1479:admots>2.0.co;2)
- Matsushita, S. (1959). A study of the morphology of ionospheric storms. *Journal of Geophysical Research*, 64(3), 305–321. <https://doi.org/10.1029/JZ064i003p00305>
- Maute, A. (2017). Thermosphere-ionosphere-electrodynamics general circulation model for the ionospheric connection explorer: TIEG-CM-ICON. *Space Science Reviews*, 212(1–2), 523–551. <https://doi.org/10.1007/s11214-017-0330-3>
- McIntyre, M. E., & Palmer, T. N. (1983). Breaking planetary waves in the stratosphere. *Nature*, 305, 593–600. <https://doi.org/10.1038/305593a0>
- Mendillo, M. (2006). Storms in the ionosphere: Patterns and processes for total electron content. *Reviews of Geophysics*, 44(4). <https://doi.org/10.1029/2005RG000193>
- Müller, J. W. (2000). Possible advantages of a robust evaluation of comparisons. *Journal of research of the National Institute of Standards and Technology*, 105(4), 551. <https://doi.org/10.6028/jres.105.044>
- Neale, R. B., Richter, J., Park, S., Lauritzen, P. H., Vavrus, S. J., Rasch, P. J., & Zhang, M. (2013). The mean climate of the Community Atmosphere Model (CAM4) in forced SST and fully coupled experiments. *Journal of Climate*, 26(14), 5150–5168. <https://doi.org/10.1175/JCLI-D-12-00236.1>
- Oyama, K.-I., Zhou, J. T., Lin, J. T., Lin, C., Liu, H., & Yumoto, K. (2014). Ionospheric response to 2009 sudden stratospheric warming in the Northern Hemisphere. *Journal of Geophysical Research: Space Physics*, 119(12), 260. <https://doi.org/10.1002/2014JA020014>
- Patra, A. K., Pavan Chaitanya, P., Sripathi, S., & Alex, S. (2014). Ionospheric variability over Indian low latitude linked with the 2009 sudden stratospheric warming. *Journal of Geophysical Research: Space Physics*, 119(5), 4044–4061. <https://doi.org/10.1002/2014JA019847>
- Pedatella, N. M., Chau, J., Schmidt, H., Goncharenko, L., Stolle, C., Hocke, K., & Siddiqui, T. (2018). How sudden stratospheric warming affects the whole atmosphere. *Eos*. <https://doi.org/10.1029/2018EO092441>
- Pedatella, N. M., & Forbes, J. M. (2010). Evidence for stratosphere sudden warming-ionosphere coupling due to vertically propagating tides. *Geophysical Research Letters*, 37(11). <https://doi.org/10.1029/2010GL043560>

- Pedatella, N. M., Fuller-Rowell, T., Wang, H., Jin, H., Miyoshi, Y., Fujiwara, H., & Goncharenko, L. (2014). The neutral dynamics during the 2009 sudden stratosphere warming simulated by different whole atmosphere models. *Journal of Geophysical Research: Space Physics*, 119(2), 1306–1324. <https://doi.org/10.1002/2013JA019421>
- Pedatella, N. M., & Liu, H. (2013). The influence of atmospheric tide and planetary wave variability during sudden stratosphere warmings on the low latitude ionosphere. *Journal of Geophysical Research: Space Physics*, 118(8), 5333–5347. <https://doi.org/10.1002/jgra.50492>
- Pedatella, N. M., Liu, H.-L., & Richmond, A. D. (2012). Atmospheric semidiurnal lunar tide climatology simulated by the whole atmosphere community climate model. *Journal of Geophysical Research*, 117(A6). <https://doi.org/10.1029/2012JA017792>
- Pedatella, N. M., Liu, H.-L., Richmond, A. D., Maute, A., & Fang, T.-W. (2012). Simulations of solar and lunar tidal variability in the mesosphere and lower thermosphere during sudden stratosphere warmings and their influence on the low-latitude ionosphere. *Journal of Geophysical Research*, 117(A8). <https://doi.org/10.1029/2012JA017858>
- Pedatella, N. M., & Maute, A. (2015). Impact of the semidiurnal lunar tide on the midlatitude thermospheric wind and ionosphere during sudden stratosphere warmings. *Journal of Geophysical Research: Space Physics*, 120(12), 740. <https://doi.org/10.1002/2015JA021986>
- Polvani, L. M., Sobel, A. H., & Waugh, D. W. (2013). The Stratosphere: Dynamics, Transport, and Chemistry (Vol. 190). John Wiley & Sons.
- Polyakova, A., Chernigovskaya, M., & Perevalova, N. (2014). Ionospheric effects of sudden stratospheric warmings in eastern Siberia region. *Journal of Atmospheric and Solar-Terrestrial Physics*, 120, 15–23. <https://doi.org/10.1016/j.jastp.2014.08.011>
- Próls, G. W. (1995). Ionospheric F-region storms. *Handbook of atmospheric electrodynamics*, 2, 195–248.
- Rajesh, P. K., Lin, C. H., Lin, C. Y., Chen, C. H., Liu, J. Y., Matsuo, T., et al. (2020). Extreme positive ionosphere storm triggered by a minor magnetic storm in deep solar minimum revealed by FORMOSAT-7/COSMIC-2 and GNSS observations. *Journal of Geophysical Research: Space Physics*, 126(2), e2020JA028261. <https://doi.org/10.1029/2020JA028261>
- Rao, J., Garfinkel, C. I., Chen, H., & White, I. P. (2019). The 2019 new year stratospheric sudden warming and its real-time predictions in multiple S2S models. *Journal of Geophysical Research: Atmosphere*, 124(21), 11155–11174. <https://doi.org/10.1029/2019JD030826>
- Richards, P. G., Fennelly, J. A., & Torr, D. G. (1994). EUVAC: A solar EUV flux model for aeronomic calculations. *Journal of Geophysical Research*, 99(A5), 8981–8992. <https://doi.org/10.1029/94JA00518>
- Rideout, W., & Coster, A. (2006). Automated GPS processing for global total electron content data. *GPS Solutions*, 10(3), 219–228. <https://doi.org/10.1007/s10291-006-0029-5>
- Roble, R. G., & Ridley, E. C. (1987). An auroral model for the NCAR thermospheric general circulation model (TGCM). *Annales Geophysicae*, 5, 369–382.
- Scherhag, R. (1952). Die explosionsartigen stratosphärenwärmungen des spät winters 1951/52. *Berichte des deutschen Wetterdienstes in der US-Zone*, 6(38), 51–63.
- Siddiqui, T. A., Maute, A., & Pedatella, N. M. (2019). On the importance of interactive ozone chemistry in Earth-System models for studying mesosphere-lower thermosphere tidal changes during sudden stratospheric warmings. *Journal of Geophysical Research: Space Physics*, 124(12), 10690–10707. <https://doi.org/10.1029/2019JA027193>
- Siddiqui, T. A., Maute, A., Pedatella, N., Yamazaki, Y., Lühr, H., & Stolle, C. (2018). On the variability of the semidiurnal solar and lunar tides of the equatorial electrojet during sudden stratospheric warmings. *Annales Geophysicae*, 36(6), 1545–1562. <https://doi.org/10.5194/angeo-36-1545-2018>
- Siddiqui, T. A., Stolle, C., & Lühr, H. (2017). Longitude-dependent lunar tidal modulation of the equatorial electrojet during stratospheric sudden warmings. *Journal of Geophysical Research: Space Physics*, 122, 3760–3776. <https://doi.org/10.1002/2016JA023609>
- Siskind, D. E., Eckermann, S. D., Coy, L., McCormack, J. P., & Randall, C. E. (2007). On recent interannual variability of the Arctic winter mesosphere: Implications for tracer descent. *Geophysical Research Letters*, 34(9). <https://doi.org/10.1029/2007GL029293>
- Smith, A. K. (2012). Global dynamics of the MLT. *Surveys in Geophysics*, 33(6), 1177–1230. <https://doi.org/10.1007/s10712-012-9196-9>
- Sunda, S., Vyas, B. M., & Khekale, P. V. (2013). Storm time spatial variations in TEC during moderate geomagnetic storms in extremely low solar activity conditions (2007–2009) over Indian region. *Advances in Space Research*, 52(1), 158–176. <https://doi.org/10.1016/j.asr.2013.03.006>
- Tapping, K. (2013). The 10.7 cm solar radio flux (F10.7). *Space Weather*, 11(7), 394–406. <https://doi.org/10.1002/swe.20064>
- Tsugawa, T., Saito, A., & Otsuka, Y. (2004). A statistical study of large-scale traveling ionospheric disturbances using the GPS network in Japan. *Journal of Geophysical Research*, 109(A6). <https://doi.org/10.1029/2003JA010302>
- van Loon, H., Jenne, R. L., & Labitzke, K. (1973). Zonal harmonic standing waves. *Journal of Geophysical Research*, 78(21), 4463–4471. <https://doi.org/10.1029/JC078i021p04463>
- Vineeth, C., Kumar Pant, T., & Sridharan, R. (2009). Equatorial counter electrojets and polar stratospheric sudden warmings - A classical example of high latitude-low latitude coupling? *Annales Geophysicae*, 27(8), 3147–3153. <https://doi.org/10.5194/angeo-27-3147-2009>
- Waters, J. W., Froidevaux, L., Harwood, R. S., Jarnot, R. F., Pickett, H. M., Read, W. G., & Walch, M. J. (2006). The Earth observing system microwave limb sounder (EOS MLS) on the aura satellite. *IEEE Transactions on Geoscience and Remote Sensing*, 44(5), 1075–1092. <https://doi.org/10.1109/tgrs.2006.873771>
- Waugh, D. W., & Randel, W. J. (1999). Climatology of Arctic and Antarctic polar vortices using elliptical diagnostics. *Journal of the Atmospheric Sciences*, 56(11), 1594–1613. [https://doi.org/10.1175/1520-0469\(1999\)056<1594:COAAP>2.0.CO;2](https://doi.org/10.1175/1520-0469(1999)056<1594:COAAP>2.0.CO;2)
- Weimer, D. R. (2005). Improved ionospheric electrodynamic models and application to calculating Joule heating rates. *Journal of Geophysical Research*, 110(A5). <https://doi.org/10.1029/2004JA010884>
- Xiong, J., Wan, W., Ding, F., Liu, L., Ning, B., & Niu, X. (2013). Coupling between mesosphere and ionosphere over Beijing through semidiurnal tides during the 2009 sudden stratospheric warming. *Journal of Geophysical Research: Space Physics*, 118(5), 2511–2521. <https://doi.org/10.1002/jgra.50280>
- Yadav, S., Pant, T. K., Choudhary, R., Vineeth, C., Sunda, S., Kumar, K., & Mukherjee, S. (2017). Impact of sudden stratospheric warming of 2009 on the equatorial and low-latitude ionosphere of the Indian longitudes: A case study. *Journal of Geophysical Research: Space Physics*, 122(10). <https://doi.org/10.1002/2017ja024392>
- Yamazaki, Y., Matthias, V., Miyoshi, Y., Stolle, C., Siddiqui, T., Kervalishvili, G., & Alken, P. (2020). September 2019 Antarctic sudden stratospheric warming: Quasi-6-day wave burst and ionospheric effects. *Geophysical Research Letters*, 47(1), e2019GL086577. <https://doi.org/10.1029/2019GL086577>
- Yamazaki, Y., Richmond, A., Maute, A., Liu, H.-L., Pedatella, N., & Sassi, F. (2014). On the day-to-day variation of the equatorial electrojet during quiet periods. *Journal of Geophysical Research: Space Physics*, 119(8), 6966–6980. <https://doi.org/10.1002/2014ja020243>
- Yamazaki, Y., Richmond, A., & Yumoto, K. (2012). Stratospheric warmings and the geomagnetic lunar tide: 1958–2007. *Journal of Geophysical Research*, (A4), 117. <https://doi.org/10.1029/2012JA017514>
- Yigit, E., & Medvedev, A. S. (2015). Internal wave coupling processes in Earth's atmosphere. *Advances in Space Research*, 55(4), 983–1003. <https://doi.org/10.1016/j.asr.2014.11.020>

- Yokoyama, N., & Kamide, Y. (1997). Statistical nature of geomagnetic storms. *Journal of Geophysical Research*, *102*(A7), 14215–14222. <https://doi.org/10.1029/97JA00903>
- Yue, X., Schreiner, W. S., Lei, J., Rocken, C., Hunt, D. C., Kuo, Y.-H., & Wan, W. (2010). Global ionospheric response observed by COSMIC satellites during the January 2009 stratospheric sudden warming event. *Journal of Geophysical Research*, *115*(A11). <https://doi.org/10.1029/2010JA015466>
- Zakharenkova, I., Astafyeva, E., & Cherniak, I. (2016). GPS and GLONASS observations of large-scale traveling ionospheric disturbances during the 2015 St. Patrick's Day storm. *Journal of Geophysical Research: Space Physics*, *121*(12), 138. <https://doi.org/10.1002/2016JA023332>
- Zhang, X., & Forbes, J. M. (2014). Lunar tide in the thermosphere and weakening of the northern polar vortex. *Geophysical Research Letters*, *41*(23), 8201–8207. <https://doi.org/10.1002/2014GL062103>
- Zhang, X., Forbes, J. M., & Hagan, M. E. (2010). Longitudinal variation of tides in the MLT region: 1. Tides driven by tropospheric net radiative heating. *Journal of Geophysical Research*, *115*(A6). <https://doi.org/10.1029/2009JA014897>